

Original Article

Cite this article: Gawęda A, Munteanu M, Siliuskas L, Kupczak K, Chew D, Waškowska A, Szopa K, Belsky V, Pantia AI, Marciniak-Maliszewska B, and Jokubauskas P. Connecting East with West: constraining polygenetic Variscan – to post-Variscan metamorphism in the Marmarosh/Maramuresh Massif, Ukraine/Romania. *Geological Magazine* 162(e4): 1–19. <https://doi.org/10.1017/S0016756824000542>

Received: 4 June 2024

Revised: 14 December 2024

Accepted: 15 December 2024

Keywords:


Eastern Carpathians; Variscan basement; geothermobarometry; U-Th-Pb dating

Corresponding author:

Aleksandra Gawęda;

Email: aleksandra.gaweda@us.edu.pl

Connecting East with West: constraining polygenetic Variscan – to post-Variscan metamorphism in the Marmarosh/Maramuresh Massif, Ukraine/Romania

Aleksandra Gawęda¹ , Marian Munteanu², Laurynas Siliuskas³, Krzysztof Kupczak¹, Dave Chew⁴, Anna Waškowska⁵, Krzysztof Szopa¹, Volodymyr Belsky⁶, Adrian Iulian Pantia², Beata Marciniak-Maliszewska⁷ and Petras Jokubauskas⁷

¹Institute of Earth Sciences, Faculty of Natural Sciences, University of Silesia in Katowice, Będzińska st.60 Sosnowiec, Poland; ²Geological Institute of Romania, Caransebeş Str. 2, RO-012271, Bucharest, Romania; ³Institute of Geology and Geography, Nature Research Centre, Akademijos 2, LT-08412 Vilnius, Lithuania; ⁴Department of Geology, School of Natural Sciences, Trinity College Dublin, Dublin 2, Dublin, Ireland; ⁵AGH University of Science and Technology, Faculty of Geology, Geophysics and Environmental Protection; al. A. Mickiewicza 30, 30-059 Kraków, Poland; ⁶M.P. Semenenko Institute of Mineralogy, Geochemistry and Ore Formation of the National Academy of Sciences of Ukraine, Palladina av. 34, Kyiv-142, Ukraine and ⁷Faculty of Geology, University of Warsaw, Żwirki i Wigury 93, 02-089 Warsaw, Poland

Abstract

This work reports the first data on the Variscan metamorphic evolution of the Marmarosh/Maramuresh massif in the Outer Eastern Carpathians. Geothermobarometry determinations coupled with U-Th-Pb dating of monazite, apatite, titanite and rutile were used to construct P-T-t paths and refine the geodynamic evolution of the pre-Alpine crystalline basement. These clockwise P-T-t paths evolve from 560–630 MPa and 515–535 °C to c. 900–1180 MPa in the north (Ukraine), while in the southern nappe (Romania), the P-T-t conditions evolve from 455–620 MPa and 545–555 °C, through to 670–745 MPa and 540–560 °C, to 910–965 MPa and 645–660 °C. The northernmost nappes were likely structurally lower relative to the southern nappes. Variscan progressive metamorphism related to nappe stacking climaxed at 350–340 Ma, as documented by U-Pb rutile and U-Th-Pb monazite dating.

In both regions, post-kinematic exhumation to 700–500 MPa, 550–630 °C MPa and then to the titanite stability field was dated at 317–327 Ma, using the U-Pb system on apatite and titanite. Subsequent Permian retrogression and exhumation was constrained to 280–290 Ma by U-Pb rutile and apatite and U-Th-Pb monazite dating. These data link the massif to the external zone of the Central European Variscides. We infer that all Variscan crystalline basement fragments in the Alps and Carpathians probably represent remnants of the same microcontinent, which was dismembered during Alpine orogenesis.

1. Introduction

The Variscides in Europe can be followed from the Iberian Peninsula in the west to the Moravo-Silesian unit in the east. Their south-eastward continuation along the margin of the East European Craton is obscured by the overthrusting of the Carpathian orogen (Fig. 1a).

The Carpathian Mountains belt in central Europe extends for more than 1300 km and is composed of the internides, deformed mainly in the Mesozoic and containing crystalline cores of Pre-Alpine (mostly Variscan) basement, and the externides that were deformed during the Cenozoic (Golonka *et al.* 2006; Schmid *et al.* 2008; Golonka *et al.* 2021 and references therein). The border between them is marked by the Pieniny Klippen Belt (Fig. 1b). The Outer Carpathians consist of a complex nappe system that verges towards the outer parts of the arcuate orogen. The nappe complex formed during Cretaceous to Neogene times due to the collision of several microplates with the European Plate. Sedimentary rocks within the nappes were deposited on the polyphase-deformed pre-Alpine basement representing the attenuated crust of the North European Platform (Ceahlau-Severin Ocean, e.g. Schmid *et al.* 2008; Matenco *et al.* 2010). In the Outer Western Carpathians, the nature of this basement is known only from olistoliths and exotic pebbles (Poprawa *et al.* 2006; Gawęda *et al.* 2019 and references therein). However, in the Eastern Carpathians, the crystalline basement underlying the Outer Eastern Carpathians sedimentary basins is exposed. Termed the Marmarosh Massif in Ukraine and the Maramuresh Massif in Romania (Fig. 1c), it is composed of Pre-Alpine rocks and is the largest

© The Author(s), 2025. Published by Cambridge University Press. This is an Open Access article, distributed under the terms of the Creative Commons Attribution licence (<https://creativecommons.org/licenses/by/4.0/>), which permits unrestricted re-use, distribution and reproduction, provided the original article is properly cited.



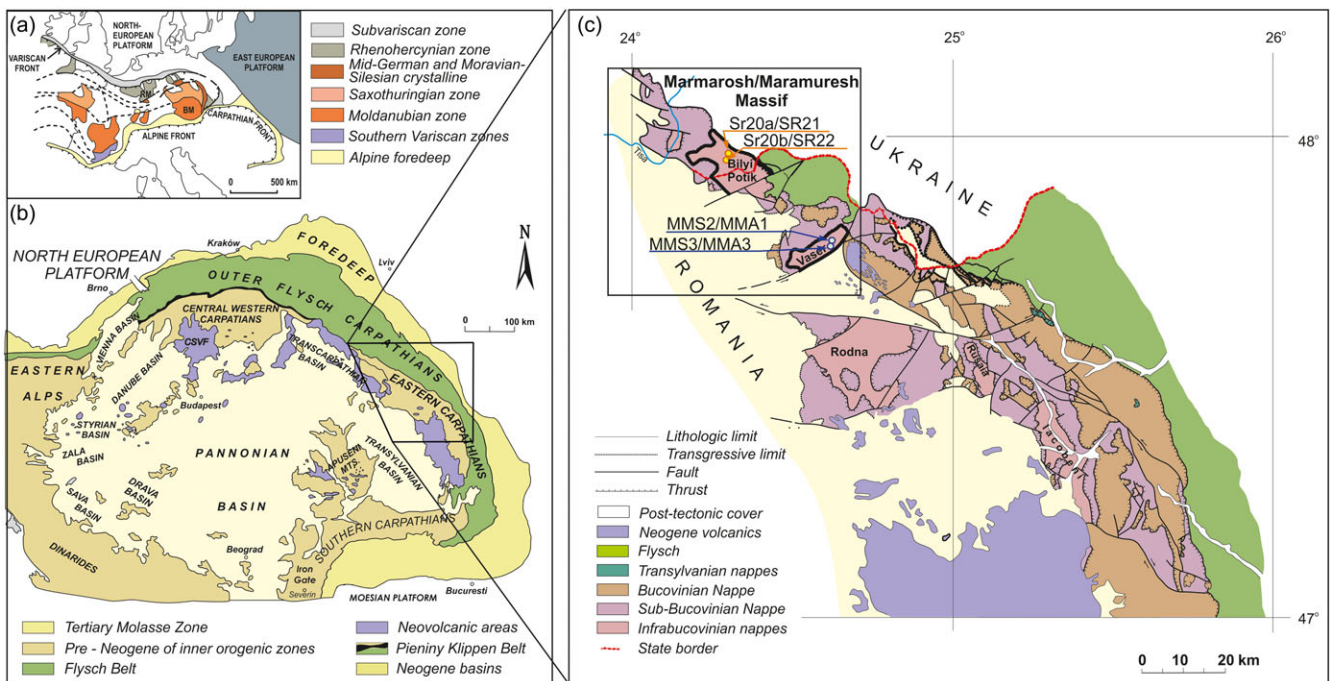


Figure 1. (a) Simplified sketch map of the Variscan belt after Franke *et al.* (1995); (b) simplified geological map of the Carpathian Mountains within the Alpine orogenic belt with (c) the Bucovinian, Sub-Bucovinian and Infrabucovinian nappes shown (compilation after Kräutner, 1988; Vodá, 2002; Matskiv *et al.* 2009).

preserved fragment of the Marmaros Ridge, a ridge of basement that was thrust NE over the Outer Carpathian flysch during Alpine collision (Tkatchuk & Gurz'ij, 1957; Kräutner, 1988). The rocks of the Marmaros/Maramuresh Massif and Marmaros Klippen Zone just represent part of the Pre-Alpine North European Platform. Reconstructing their geological history not only aids our understanding of the Outer Eastern Carpathians basement but also the geotectonic development of the SW margin of Baltica. The Marmaros Ridge is believed to represent the eastern prolongation of the Silesian Ridge of the Outer Western Carpathians. The Silesian Ridge separated the Silesian and Magura basins during the late Mesozoic and Paleogene and is inferred to be the source of the coarse detritus deposited in both basins (Săndulescu, 1988; Oszczytko *et al.* 2005; Golonka *et al.* 2021; Bónová *et al.* 2019).

This study aims to decipher the Pre-Alpine metamorphic history of the Marmaros/Maramuresh massifs (the Bilyipotik Nappe in Ukraine; the Bretila Group of the Vaser Infrabucovinian Nappe in Romania), where amphibolite-facies pelitic schists with amphibolite intercalations predominate. Multi-tool petrochronology was applied, including U-Pb apatite, rutile and titanite dating for amphibolites and for interleaved metapelites U-Th-Pb CHIME dating of monazite and U-Pb apatite and rutile dating. Geochronological data are coupled with thermodynamic modeling of stable mineral assemblages, which allow us to reconstruct P-T-t paths of the metamorphic units and to refine the geodynamic evolution of the pre-Alpine basement of the Outer Eastern Carpathians.

2. Geological setting and sampling

The crystalline segment, called Marmaros/Maramuresh Massif, is a constituent of northernmost part of the Outer Eastern Carpathians, located north-east of the Pieniny Klippen Belt (Kräutner & Bindea, 2002; Munteanu & Tatu, 2003). The Pre-Alpine terranes of the Eastern Carpathians were subjected to Aptian-Albian thrusts that

generated Alpine-age nappes with metamorphic (crystalline) basements and dominantly Mesozoic sedimentary cover, which Uhlig (1907) termed the Crystalline-Mesozoic Zone (CMZ).

In the Ukrainian part of the massif two crystalline units, the Bilyipotik and Dilove nappes, are recognized (Matskiv *et al.* 2009) (Figs. 1c, 2a). The Bilyipotik Nappe is composed of amphibolite-facies metamorphic rocks of the Bilyipotik suite (1300 m) which consist of orthogneisses and mica-schists, locally garnet-bearing, intercalated with rare amphibolites and marble lenses. They are structurally overlain by weakly metamorphosed rocks of the Rozyn suite (phyllites, marbled limestones and dolomites up to 600 m thick) and predominantly unmetamorphosed volcanic-sedimentary formations (up to 900 m). The structurally higher Dilove Nappe is composed of greenschist-facies metamorphic rocks, including Neoproterozoic metapelites/meta-tuffs and felsic to intermediate metavolcanics of early Caledonian age, connected to the closure of the easternmost Tornquist Ocean on the margin of Baltica (Munteanu & Tatu, 2003; Oszczytko *et al.* 2005; Gawęda *et al.* 2022).

In the Romanian part of the Eastern Carpathians, the following Alpine nappes with pre-Alpine basement are identified: the Bucovinian Nappe, Sub-Bucovinian Nappe and several Infrabucovinian Nappes (Săndulescu, 1984; 1994). The metamorphic basement of the Bucovinian and Sub-Bucovinian nappes is made up of the following pre-Alpine nappe stack from top to bottom (Fig. 2b):

- The Rarău Nappe comprised of the amphibolite-facies Bretila Group (garnet ± staurolite metapelitic schists and gneisses, orthogneisses, amphibolites).
- The Putna Nappe comprising the greenschist-facies Tulgheş Group (chlorite-sericite-quartz schists ± graphite ± albite ± rutile pseudomorphs on ilmenite, graphitic metacherts, metarhyolites, felsic metatuffs, metagraywackes, rare limestones and metamorphosed mafic rocks).

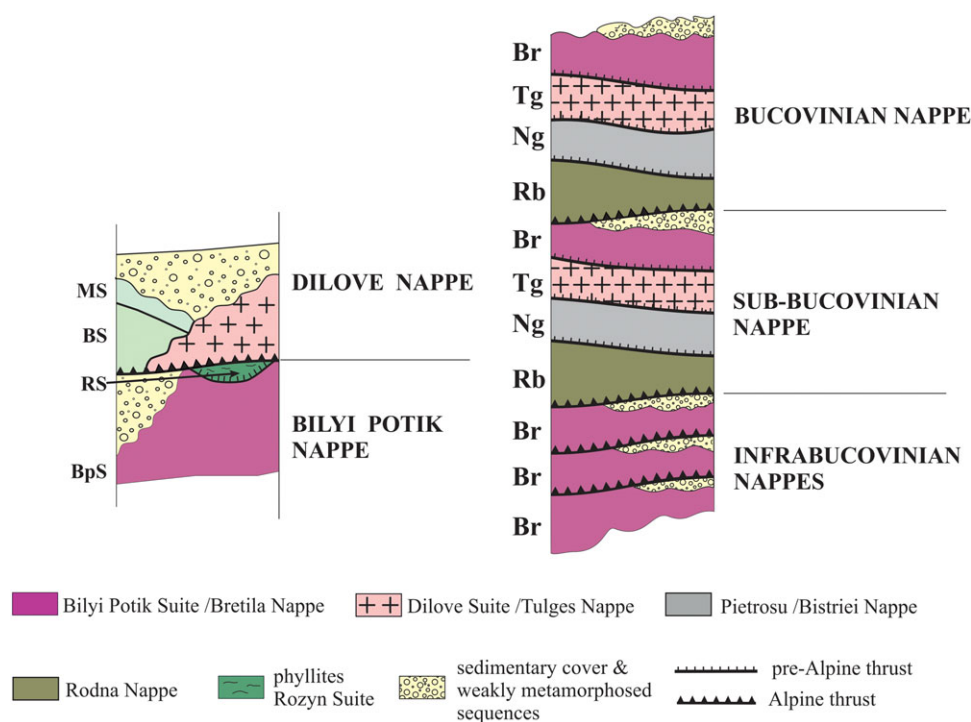


Figure 2. The tectonostratigraphy of the metamorphic terranes of the Eastern Carpathians (not to scale). Abbreviations of the metamorphic sequences in the Romanian and Ukrainian part of the Eastern Carpathians: BS – Berlebach Suite; MS – Megura Suite; RS – Rozyn Suite; BpS – Bilyi Potik Suite; Br – Bretila Group; Ng – Negrişoara Group; Rb – Rebra Group; Tg – Tulgeş Group.

- The Pietrosu Bistriței Nappe consisting of the Pietrosu Bistriței metarhyodacite and the Negrişoara Group (intensely deformed micaschists and gneisses, with amphibolite and carbonate intercalations; Balintoni & Balica, 2013).
- The Rodna Nappe, consists of the amphibolite-facies Rebra Group, which is comprised predominantly of micaschists and pelitic gneisses with amphibolites, dolomites and limestones (\pm tremolite \pm wollastonite \pm diopside, quartzite \pm graphite).

The Infrabucovinian Nappe is exposed only in tectonic windows and is composed of metamorphic basement attributed to the Bretila Group and Mesozoic \pm Permian sedimentary cover. In this research, we investigated rocks of the Infrabucovinian Bretila Group from the Vaser and Bilyipotik tectonic windows. We sampled garnet-staurolite-mica schists from the Bilyipotik Nappe (SR20Ca and SR20Cb) and two interleaving amphibolites (SR21 and SR22), near a tourist path following the Bilyi Potik stream (Figs. 1c, 3a; Table 1) in the Ukrainian part of the Marmarosh Massif. From the Romanian part of the Maramuresh Massif (Vaser window), garnet-bearing MMS-2 and MMS-3 schists were sampled with two interleaving amphibolites MMA1 (associated with MMS2) and MMA3 (associated with MMS3) outcropping in the Bretila Group, Infrabucovinian Vaser Nappe (Figs. 1c, 2b, 4a, b; Table 1).

3. Analytical techniques

3. a. Microscopy and electron probe micro-analyses (EPMA)

Petrographic analyses of thin sections were undertaken at the Institute of Earth Sciences in the University of Silesia using Olympus BX-51 and SX-10 microscopes to describe mineral parageneses and to constrain the textural position of the minerals studied, including monazite, apatite, titanite and rutile.

Microprobe analyses of the main rock-forming and accessory minerals were carried out at the Laboratory of Electron Microscopy, Microanalysis and X-Ray Diffraction (Faculty of

Geology, University of Warsaw, Poland), using a CAMECA SX-100 electron microprobe. The analytical conditions employed an accelerating voltage of 15 kV, a beam current of 20 nA, counting times of 20–30 s for peak and 10–15 s for background and a beam diameter of 1–5 μ m. Reference materials, analytical lines, diffracting crystals, mean detection limits (in wt%) and uncertainties were as follows: rutile – Ti ($K\alpha$, PET, 0.03, 0.05), diopside – Mg ($K\alpha$, TAP, 0.02, 0.11), Si – ($K\alpha$, TAP, 0.02, 0.21), Ca – ($K\alpha$, PET, 0.03, 0.16), orthoclase – Al ($K\alpha$, TAP, 0.02, 0.08), and K ($K\alpha$, PET, 0.03, 0.02), albite – Na ($K\alpha$, TAP, 0.01, 0.08), hematite – Fe ($K\alpha$, LIF, 0.09, 0.47), rhodonite – Mn ($K\alpha$, LIF, 0.03, 0.10), phlogophite – F ($K\alpha$, TAP, 0.04, 0.32), tugtupite – Cl ($K\alpha$, PET, 0.02, 0.04), Cr_2O_3 – Cr ($K\alpha$, PET, 0.04, 0.01), ZirconED2 – Zr ($L\alpha$, PET, 0.01, 0.01), Nb_2O_5 -MAC – Nb ($L\alpha$, PET, 0.09, 0.01), V_2O_5 – V ($K\alpha$, LIF, 0.02, 0.01), YPO_4 – Y ($L\alpha$, TAP, 0.05, 0.05), CeP_5O_{14} – Ce ($L\alpha$, LPET, 0.09, 0.02), $NdGaO_3$ – Nd ($L\alpha$, LIF, 0.31, 0.24), ThO_2 – Th ($M\alpha$, LPET, 0.09, 0.09) and UO_2 – U ($M\alpha$, LPET, 0.16, 0.13).

3. b. Whole-rock chemical analyses

Whole-rock analyses were undertaken by X-ray fluorescence (XRF) at Bureau Veritas Minerals (Canada). Preparation involved lithium borate fusion and dilute digestions, while LOI (loss on ignition) was determined at 1000 °C. Uncertainties for most of elements are 0.01%, except for SiO_2 which is 0.1%.

3. c. U-Th-Pb monazite dating

Due to the abundance of small monazite crystals (20 – 40 μ m in size) in the metapelitic samples, we undertook in situ U-Th-Pb monazite dating by electron probe micro-analyses (EPMA) to define the age of metamorphism. Monazite chemical dating was undertaken on a CAMECA SXFiveFE electron microprobe equipped with a Schottky emitter at the Laboratory of Electron Microscopy, Microanalysis and X-Ray Diffraction (Faculty of Geology, University of Warsaw, Poland) at 15 kV with an

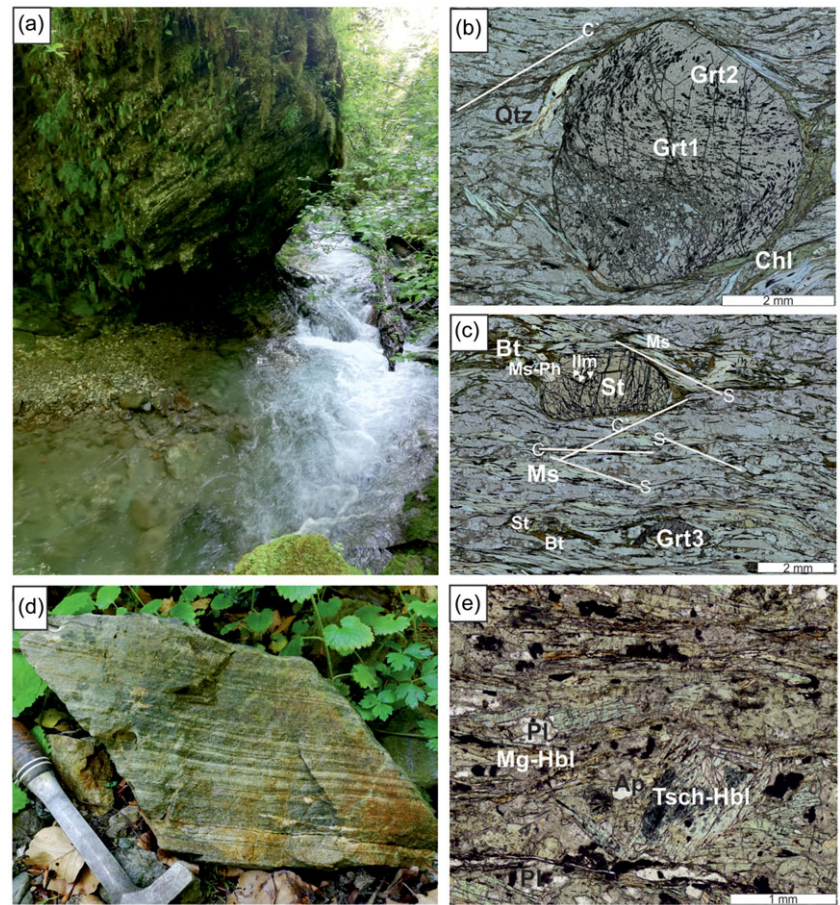


Figure 3. Textural relationships in the Marmarosh Massif (Ukraine). (a) Field photograph showing the sampling locality of samples SR20C and SR21, (b) photomicrograph showing snowball garnet (Grt); (c) photomicrograph of staurolite (St) and post-tectonic garnet (Grt) and a foliation defined by muscovite (Ms) and biotite (Bt); (d) striped amphibolite sample SR22 with a foliation defined by plagioclase-quartz segregations; (e) Mg-hornblende (Mg-hbl) overgrowing tschermakitic hornblende (Tsch-Hbl) in sample SR22.

unregulated beam current of 100 nA. Beam current stability within a one hour window was within $\pm 0.5\%$, except for the last run (for sample MMS2) where beam drift exceeded 1% for 12 min). No statistically significant biases due to beam drift were found.

The analytical setup for monazite dating employs simultaneous measurement of Pb (120 s peak/ 120 s background) on the second WDS spectrometer (LPET), with Th (90 s peak/ 50 s background) and U (120 s peak/120 s background) on fifth spectrometer (LPET). Reference materials, analytical lines, diffracting crystals, mean detection limits (in wt%) and uncertainties are given in Supplementary Table 1. U, Pb, Th measurements were done at differential pulse height analysis modes with narrow energy window which improves signal-to-noise ratio and minimizes higher order interferences, however, does not eliminates peak overlaps completely. The monazite dating setup has 62 peak-overlap correction entries defined, including the most relevant peak overlap corrections for dating – Pb $M\alpha$ by Y $L\gamma_2$, Th $M\alpha$ by 2nd order Pr, Ce and Sm L lines and U $M\alpha$ by Pb $M2N4$. Monazite from Namaqualand (South Africa Republic) was measured as an age standard. Its mean age from 30 EPMA points is 1046 ± 3 Ma, which statistically does not differ from the published $206\text{Pb}/238\text{U}$ age of 1046.5 ± 7.1 Ma (LA-ICP-MS, Liu *et al.* 2012).

3. d. Apatite, rutile and titanite separation and imaging

Apatite, rutile and titanite crystals from four amphibolite and one metapelite samples were separated using standard density separation techniques (crushing, sieving, washing and panning) at the Institute of Geological Sciences at the Polish Academy of

Sciences, Kraków, Poland. Mineral phases were hand-picked under a binocular microscope, cast in 25 mm diameter epoxy resin mounts and then ground and polished to expose the grain interiors. Mineral textures were then imaged using back-scattered electron (BSE) and cathodoluminescence (CL) detectors on a FET Philips 30 scanning electron microscope with a 15 kV accelerating voltage and a beam current of 1 nA at the Faculty of Natural Sciences, University of Silesia in Katowice, Poland.

3. e. Apatite, titanite and rutile LA-ICP-MS U-Pb dating

LA-ICP MS U-Pb age and trace element data were acquired using a Photon Machines Analyte Excite 193 nm ArF excimer laser-ablation system with a HelEx 2-volume ablation cell coupled to an Agilent 7900 ICP MS at the Department of Geology, Trinity College Dublin. The instruments were tuned using NIST612 standard glass to yield Th/U ratios of unity and low oxide production rates (ThO^+/Th^+ typically $< 0.15\%$). A repetition rate of 11 Hz and a circular spot of 60 μm (apatite), 47 μm (titanite) and 45 μm (rutile) were employed. A quantity of 0.4 l min^{-1} He carrier gas was fed into the laser cell, and the aerosol was subsequently mixed with 0.6 l min^{-1} Ar make-up gas and 11 ml min^{-1} N_2 . Each analysis comprised 27 s of ablation and 12 second washout, the latter portions of which were used for the baseline measurement.

The data reduction of the raw U-Th-Pb isotopic data was undertaken using the freeware IOLITE package (Paton *et al.* 2011) with the 'VizualAge UcomPbine' data reduction scheme (Petrus & Kamber, 2012; Chew *et al.* 2014) which can account for the presence of variable common Pb in the primary age reference

Table 1. GPS co-ordinates of the sampling points

Sample No	Latitude	Longitude
Ukraine		
SR20b	47° 55' 54,7''	24° 15' 25,9''
SR21 SR22	47° 55' 51,7''	24° 15' 23,5''
Romania		
MMS2	47° 44' 00,8''	24° 32' 46,5''
MMA1	47° 43' 59,8''	24° 32' 48,3''
MMS3 MMA3	47° 43' 46,1''	24° 33' 39,0''

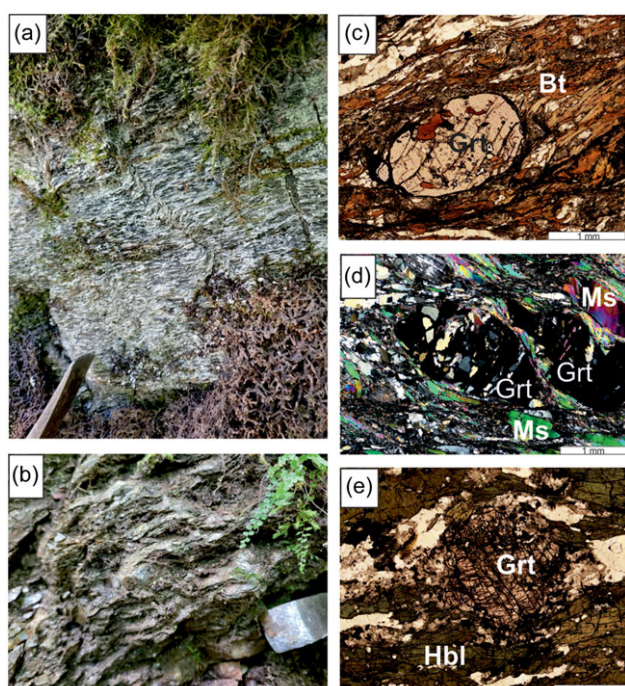


Figure 4. Textural relationships in the Maramuresh Massif (Romania). (a) Field photograph of amphibolite MMA1; (b) field photograph of metapelite MMS2; (c) photomicrograph of garnet-bearing metapelite sample MMS2, (d) photomicrograph of garnet-bearing metapelite sample MMS3 with an S-C fabric; (e) photomicrograph of the amphibolite sample MMA3 with garnet porphyroblasts surrounded by Mg-hornblende. Abbreviations as in Figure 3.

material. Common Pb in the apatite, titanite and rutile standards was corrected using the ^{207}Pb -based correction method. Conventional sample-standard bracketing was then applied to account for both downhole fractionation and long-term drift in isotopic or elemental ratios by normalizing all ratios to those of the U-Th-Pb reference materials. All apatite, rutile and titanite ages were calculated offline using the Isoplot plug-in for Excel (Ludwig, 2012).

Twenty-nine isotopes (^{31}P , ^{35}Cl , ^{43}Ca , ^{51}V , ^{55}Mn , ^{88}Sr , ^{89}Y , ^{90}Zr , ^{139}La , ^{140}Ce , ^{141}Pr , ^{146}Nd , ^{147}Sm , ^{153}Eu , ^{157}Gd , ^{159}Tb , ^{163}Dy , ^{165}Ho , ^{166}Er , ^{169}Tm , ^{172}Yb , ^{175}Lu , ^{204}Pb , ^{206}Pb , ^{207}Pb , ^{208}Pb , ^{232}Th and ^{238}U) were acquired for apatite. NIST612 standard glass was used as the apatite trace-element reference material with ^{43}Ca employed as an internal elemental standard, and a crushed aliquot of Durango apatite that has been characterized by solution quadrupole-ICP-MS analyses (Chew *et al.* 2016) was used as the apatite

trace-element secondary standard. For U-Pb apatite analyses, the Madagascar natural mineral standard (Thomson *et al.* 2012) was used as the primary age reference material, using a *c.* 1 cm sized crystal of Madagascar apatite which has yielded a weighted average ID-TIMS concordia age of 473.5 ± 0.7 Ma (unpublished data from the study of Cochrane *et al.* 2014). McClure Mountain syenite apatite (total Pb/U isochron age of 525.3 ± 1.7 Ma; Krestianinov *et al.* 2021) and Durango apatite (linear 3-D isochron age of 32.683 ± 0.050 Ma; Paul *et al.* 2021) were used as secondary standards and yielded ^{207}Pb -corrected ages of 522.9 ± 56.8 Ma (MSWD = 1.8) and 32.49 ± 0.94 Ma (MSWD = 1.4), respectively, using a $^{207}\text{Pb}/^{206}\text{Pb}$ value of 0.874 derived from an apatite ID-TIMS total U-Pb isochron (Krestianinov *et al.* 2021) and a $^{207}\text{Pb}/^{206}\text{Pb}$ value derived from the Stacey & Kramers (1975) terrestrial Pb evolution model at 32.68 Ma.

For titanite, thirteen isotopes (^{43}Ca , ^{48}Ti , ^{89}Y , ^{90}Zr , ^{140}Ce , ^{172}Yb , ^{200}Hg , ^{204}Pb , ^{206}Pb , ^{207}Pb , ^{208}Pb , ^{232}Th and ^{238}U) were acquired. The primary titanite standard used in this study is OLT1 titanite, which has yielded a TIMS concordia age of 1014.8 ± 2.0 Ma (Kennedy *et al.* 2010). BLR titanite Aleinikoff *et al.* (2002), which has yielded an ID-TIMS age of 1048.0 ± 0.7 Ma, was used as the titanite secondary LA-ICP-MS age reference material and yielded weighted average ^{207}Pb -corrected ages of 1013.5 ± 8.9 Ma (MSWD = 0.65) and 1028 ± 14 Ma (MSWD = 1.4).

R10 was employed as the primary standard, and R19 (ID-TIMS date of 489.5 ± 0.9 Ma; Zack *et al.* 2011) and R13 (U-Pb SHRIMP age of 5045 ± 4 Ma, Schmitt & Zack, 2012) were employed as secondary standards and treated as unknowns during data reduction and yielded weighted average ^{207}Pb -corrected ages of 489.4 ± 2.6 Ma and 505 ± 16 Ma, respectively.

3. f. Thermodynamic modelling

Phase diagrams were constructed using the bulk rock chemical compositions of the representative metapelite samples SR20b and MMS3 (Table 2). For this, THERIAK DOMINO software package (dataset tcds62cid; de Capitani & Brown, 1987; de Capitani & Petrakakis, 2010) was used in the MnNCKFMASHT system under fully water-saturated conditions with the internally consistent dataset of Holland and Powell (2011). The following phases and a-X models were implemented: clinopyroxene and melt (Green *et al.* 2016), biotite, cordierite, garnet, ilmenite, staurolite, spinel and orthopyroxene (White *et al.* 2014a; 2014b), chlorite (White *et al.* 2014a; 2014b; Powell *et al.* 2014), epidote (Holland & Powell, 2011), feldspar (Holland & Powell, 2003) and white mica (Coggon & Holland, 2002). Quartz, titanite, rutile, sillimanite, andalusite, kyanite and water were treated as pure phases. Isoleths for garnet and plagioclase endmembers and Si in white mica were plotted. Additionally, we apply the Ti-in-biotite geothermometer after Henry *et al.* (2005) and the Zr-in-rutile geothermometer (Zack *et al.* 2004) for additional geothermometry constraints, while the amphibole-plagioclase NaSi-CaAl geobarometric approach (Molina *et al.* 2015) and Ti-in-calcium amphibole thermometry (Liao *et al.* 2021), coupled with the classical Blundy & Holland (1990) thermobarometer, were applied to amphibolites. The revised nomenclature of amphiboles (Leake *et al.* 2004) was applied.

4. Results

4. a. Petrography and mineral chemistry

4. a.1. Bilyipotik Nappe (Ukraine) – metapelites

The metapelite sample (SR20c) is characterized by the presence of garnet and staurolite porphyroblasts, containing mineral

Table 2. Chemical composition of the whole-rock metapelitic samples from the Marmarosh Massif (Ukraine/Romania)

Sample No	LoD	SR20b	MMS2	MMS3
SiO ₂	0.10	63.80	64.90	62.48
TiO ₂	0.01	1.06	0.77	0.81
Al ₂ O ₃	0.01	17.3	18.18	18.88
Fe ₂ O _{3T}	0.04	7.9	6.79	6.17
MnO	0.01	0.21	0.15	0.13
MgO	0.01	1.79	1.43	1.57
CaO	0.01	1.26	1.46	1.48
Na ₂ O	0.01	2.39	1.52	1.6
K ₂ O	0.01	2.47	3.87	4.16
P ₂ O ₅	0.01	0.14	0.09	0.1
LOI	–	2.08	1.84	2.08
Total		100.40	101.00	99.46

inclusions, and a biotite + muscovite + quartz + plagioclase matrix (Figs. 3b, c). Accessory phases are ilmenite, rutile, Ca (F, OH)-apatite, monazite-Ce and zircon.

Garnet crystals of 1 to 4 mm in size (Fig. 3b) are zoned with respect to Fe, Mg, Ca and slightly Mn (Figs. 5a–d, f), and they are classified as almandine, with subordinate substitutions of grossular, pyrope and spessartine. The garnet core composition is Alm_{65–60}Gros_{24–20}Py_{6.5–3.0}Spess_{8–15}, while the rim composition is Alm_{80–79}Gros_{12.0–9.5}Py_{10.3–7.0}Spess_{0.7–2.0} (Supplementary Table 2a). They contain abundant inclusions of ilmenite, plagioclase, quartz, zircon and monazite while rutile intergrown with ilmenite is found in the rims also. Inclusions define the snowball structure of the garnet (Fig. 3b). Plagioclase, both in the matrix and as inclusions in garnet, is oligoclase (An_{22–27}). Biotite crystals are often chloritized. Unaltered biotite exhibits beige-brick-red pleochroism, with #mg in the range of 0.47–0.48 and Ti in the range of 0.19–0.20 a.p.f.u. (Table 3). Ilmenite (Ilm), mostly intergrown with rutile (Rt), occurs both as inclusions in garnet porphyroblasts and as a component of the matrix (Figs. 5a, e). All ilmenite crystals exhibit Mn substitution (Table 5).

Staurolite porphyroblasts, up to 1 mm in size, are parallel to the foliation defined by mica group minerals and mineral lineation (Fig. 3c). A slight chemical zonation due to Mg-Fe exchange is observed, but, in general, the staurolite is the Fe-variety (Supplementary Table 3). It is associated with small garnet crystals (Grt 3 – Alm_{75–73}Gros_{13.6}Py_{13–11}Spess_{2–10}; Fig. 3c; Supplementary Table 2a). Muscovite exhibits relatively small phengite contents (Si = 6.097–6.114 a.p.f.u. coupled with Mg = 0.075–0.091 a.p.f.u.) and elevated Na contents (0.376–0.576 a.p.f.u.; Table 4). Chlorite with an Fe/(Fe+Mg) ratio in the range of 0.54–0.61 (classified as ripidolite – brunsvigite; Table 6) replaces primary biotite. Among accessory phases, zircon crystals are rare. Monazite crystals from c. 20 µm to 80 µm in length are present both as inclusions in garnet and in the matrix (Figs. 5e, g, h). Most of them are unaltered, only locally overgrown by REE-rich epidote (Fig. 5h; Supplementary Table 1). Apatite crystals are quite common but show intensive recrystallization.

Four main mineral assemblages can be defined, related to kinematic history of the rock. Remanence of assemblage 1 (prograde) is defined by garnet core (Grt 1) and inclusions hosted within it (plagioclase, quartz, ilmenite, zircon and monazite).

Assemblage 2 (peak of metamorphism) is defined by garnet rims (Grt 2) with inclusions of plagioclase, quartz and rutile in it and muscovite in the matrix. Assemblage 3 (post-kinematic) is represented by staurolite, containing inclusions of ilmenite, biotite and quartz and overgrown by biotite with similar composition and muscovite, as well as small elongated garnet (Grt 3; Fig. 3c). Assemblage 4 (retrograde) is composed of secondary minerals: post-biotite chlorite, RE-epidote, apatite and carbonate minerals (Figs. 3b, c; 5h), and which continued to grow during decompression. Shearing was probably continuous as evidence by inclusion trails in garnet porphyroblasts and S-C structures in the rock (Figs. 3b, c).

4. a.2. Bilyipotik Nappe (Ukraine) – amphibolites

The amphibolites (SR21 & SR22) show a strong metamorphic foliation and lineation, highlighted by dark and leucocratic layers (Fig. 3d). Amphibole group minerals, being the major mineral components, are classified as tschermakitic hornblende – aluminotschermakitic hornblende – magnesio-hornblende (Supplementary Table 4a) and coexist with plagioclase (An_{35–27}), accessory ilmenite, (Ca,F)-apatite and zircon. Tschermakitic- and aluminotschermakitic hornblende forms porphyroblasts, together with andesine plagioclase, while magnesio-hornblende, equilibrated with oligoclase and ilmenite, postdates it and defines the foliation and lineation (Fig. 3e). Accessories are represented by rare zircon and abundant Ca-F apatite. Ilmenite (Fe_{1.00–0.93}Mn_{0.08–0.02}TiO₃; Table 5) is replaced by titanite and is locally subidioblastic (Table 5). Rare secondary actinolite and actinolitic hornblende, together with common epidote and chlorite, replace amphibole and plagioclase. The rock is locally cut by carbonate veinlets up to 0.5 mm thick.

4. a.3. Bretila group, vaser infrabuconian Nappe (Romania) – metapelites

The biotite-garnet schists (MMS2 & MMS3) from the Bretila Group are medium-grained, with garnet porphyroblasts ranging from 0.1 to 3.0 mm in size (Figs. 4b–d).

Garnets are classified as almandine and are zoned with respect to Fe, Mn, Mg and Ca. In the metapelite sample, MMS-2 garnets (0.1–0.5 mm in size) are almost homogeneous, with core composition of Alm_{73–72}Gros₇Py_{12–11}Spess_{6–5}, and rims have a composition of Alm_{75–74}Gros₇Py_{13–12}Spess_{6–7}. In sample MMS-3, the garnet (1.5–3 mm in diameter) has cores compositions of Alm_{70–66}Gros_{19–10}Py_{11–8}Spess_{11–6}, while the rim composition is Alm_{65–63}Gros_{22–18}Py_{14–8}Spess_{7–2} (Supplementary Table 2b). The garnets contain inclusions of quartz, biotite, oligoclase, ilmenite and rutile (Figs. 4c, d). Mineral inclusions and minerals in the matrix do not differ in chemical composition. Biotite shows a characteristic beige-brown pleochroic scheme (Fig. 4c), with #mg in the range of 0.42–0.46 and Ti in the range of 0.18–0.20 a.p.f.u. (Table 3). In muscovite, defining the S-C fabric (Fig. 4d) elevated phengite and elevated Na contents were noted (0.21–0.25 a.p.f.u.; Table 4). Ilmenite exhibits Mn substitution and is locally replaced by titanite (Table 5). Accessory phases are monazite, partly replaced by epidote+apatite coronas, rare zircon, long-prismatic rutile and apatite of yellow to green CL (Figs. 6a–c, e). Rutile is characterized by Zr contents ranging from 210–381 ppm, Cr from 55.6–1494 ppm, Nb from 1455–3850 ppm and Hf from 1.73–10.2 ppm. (Supplementary Table 5).

Remnants of the prograde mineral assemblage (Assemblage 1) are represented by garnet cores and mantles (Grt1) and inclusions (biotite, plagioclase, ilmenite? and rutile). The peak assemblage (Assemblage 2) is Grt2 + Ms + Pl + Bt + Rt1 + Qtz. The post-kinematic mineral assemblage (Assemblage 3) is defined by biotite,

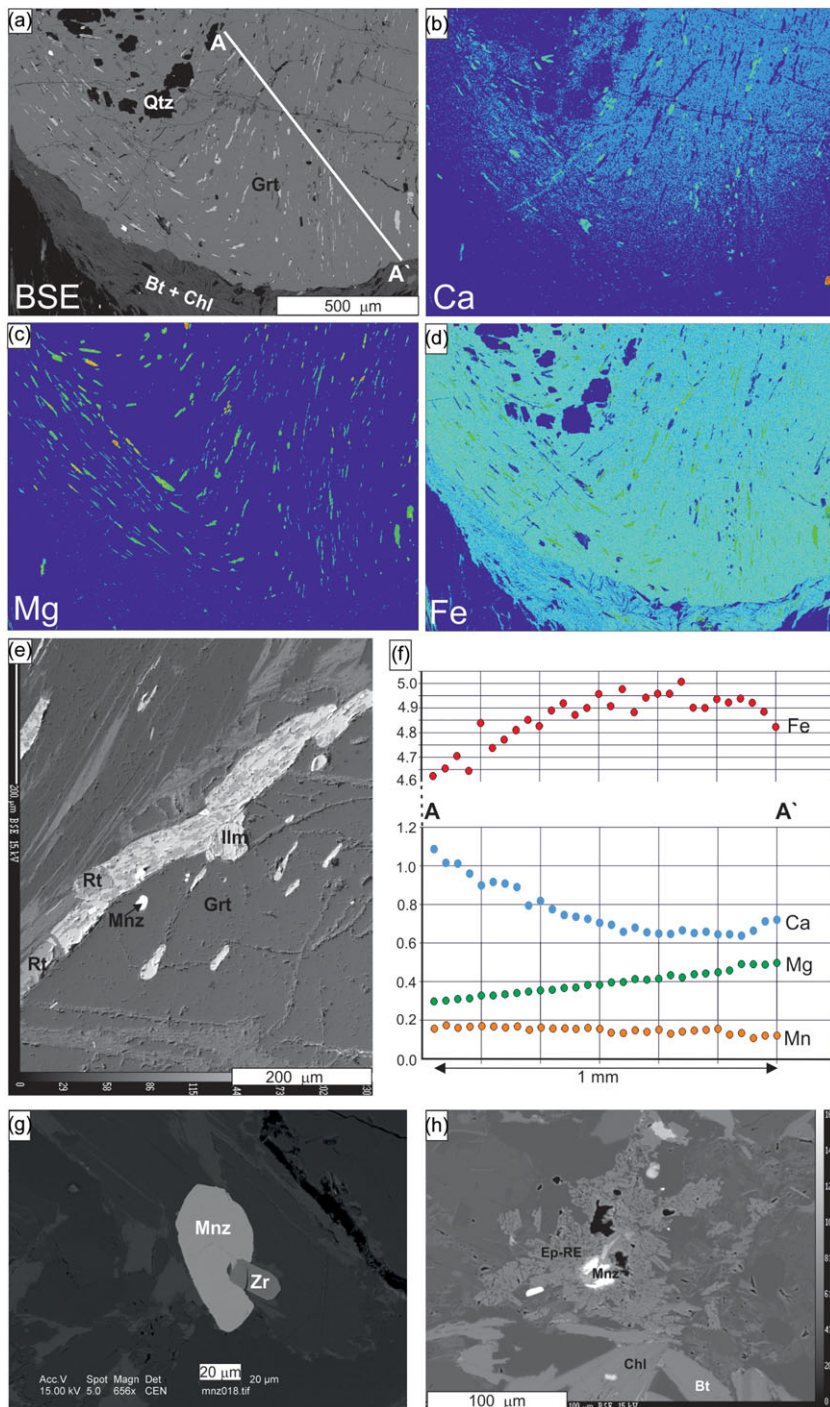


Figure 5. BSE images from metapelite sample SR20C of the Marmorosh Massif (Ukraine): (a) portion of a garnet porphyroblast with inclusions defined by ilmenite+rutile (Ilm, Rt), monazite (Mnz) and quartz (Qtz); (b – d) chemical distribution of Ca, Mg and Fe in same area as a); (e) intergrowths of rutile (Rt) and ilmenite (Ilm) on the rim of a garnet porphyroblast; (f) chemical transect along the garnet porphyroblast in (a); (g) monazite Mnz1 and zircon from metapelite sample SR20C; (h) monazite Mnz2 rimmed by REE-epidote from sample SR20C.

muscovite, ilmenite, monazite, titanite and apatite. The final late retrograde assemblage (Assemblage 4) is formed by secondary minerals: chlorite, rare earth-epidote + apatite and rutile (Rt2). All mineral assemblages grew during continuous ductile shearing, as evidenced by the inclusion trails in garnets and associated S-C fabric (Figs. 4c, d).

4. a.4 Brettila group, Vaser infrabuconian Nappe (Romania) – Amphibolites

The amphibolite interleaved with the metapelites exhibits a strong foliation and mineral lineation (Fig. 4a). In the striped amphibolite sample MMA1, the main mineral phases (amphiboles) can be

classified as Mg-hornblende (porphyroblasts) to tschermakitic hornblende and ferrian tschermakitic hornblende, which defines the foliation and postdates Mg-hornblende. Minor actinolite and actinolitic hornblende rims were found around Mg-hornblende (Supplementary Table 4b). Plagioclase is replaced by sericite + albite. Accessories are represented by abundant rutile locally replaced by ilmenite and titanite, while ilmenite is replaced by titanite (Fig. 6d).

In the garnet-bearing amphibolite sample MMA3, magnesio-hornblende to tschermakitic hornblende (Supplementary Table 4b) and oligoclase-andesine (An₂₆₋₃₃) are the main components, enclosing accessory almandine-grossular-rich garnet crystals

Table 3. Chemical compositions, crystal-chemical formulae and calculated crystallization temperatures (Henry *et al.*, 2005) of representative biotite crystals from metapelites

Sample No	Component	LoD	SR20A (UKR)			MMS2 (ROM)			MMS3 (ROM)		
			Bt1	Bt2	Bt3	Bt1	Bt2	Bt3	Bt1	Bt2	Bt3
	SiO ₂	0.04	35.29	36.21	35.19	35.13	35.47	35.46	35.15	35.17	35.02
	TiO ₂	0.06	1.31	1.49	1.75	1.80	1.70	1.74	1.50	1.62	1.71
	Al ₂ O ₃	0.03	20.04	20.07	19.76	18.94	18.90	19.10	18.22	18.34	17.87
	Cr ₂ O ₃	0.01	b.d.l.	b.d.l.	b.d.l.	0.02	0.04	0.06	0.05	0.06	0.05
	FeO	0.15	19.43	18.78	20.36	19.56	19.76	19.91	22.18	21.49	22.40
	MgO	0.02	9.34	9.49	9.36	9.96	9.63	9.71	9.14	9.28	9.26
	MnO	0.02	0.10	0.06	0.01	0.11	0.10	0.12	0.16	0.17	0.16
	Na ₂ O	0.04	0.43	0.43	0.31	0.07	0.07	0.12	0.03	0.08	0.05
	K ₂ O	0.05	8.57	8.95	8.86	8.69	8.95	8.99	8.91	9.39	9.06
	BaO	0.01	0.07	0.01	0.04	0.10	0.13	0.07	0.04	0.05	0.04
	Total		94.58	95.49	95.64	94.38	94.75	95.28	95.38	95.64	95.62
Crystal-chemical formulae recalculated for 22 O ²⁻											
	Si		5.462	5.200	5.359	5.402	5.441	5.433	5.439	5.402	5.427
	Al ^{iv}		2.538	2.800	2.641	2.598	2.559	2.567	2.561	2.598	2.573
	Al ^{vi}		1.030	0.737	0.905	0.835	0.873	0.882	0.762	0.721	0.691
	Ti		0.169	0.138	0.201	0.208	0.196	0.201	0.175	0.188	0.199
	Cr		–	–	–	0.003	0.005	0.007	0.006	0.007	0.006
	Fe		2.369	3.285	2.593	2.519	2.534	2.552	2.87	2.76	2.903
	Mg		2.133	1.958	2.124	2.284	2.203	2.217	2.109	2.126	2.139
	Mn		0.008	0.01	0.001	0.014	0.013	0.015	0.021	0.022	0.021
	Na		0.126	0.023	0.093	0.02	0.02	0.036	0.009	0.023	0.014
	K		1.625	1.423	1.566	1.704	1.751	1.757	1.759	1.84	1.791
	Ba		0.001	0.001	0.002	0.006	0.008	0.004	0.003	0.003	0.002
	#mg		0.461	0.474	0.450	0.476	0.465	0.465	0.424	0.435	0.424
	T _{H(2005)}		513	545	578	590	575	580	540	560	570

Abbreviations: b.d.l. – below detection limit; #mg = Mg/(Mg+Fe); T_H = temperature of crystallization (after Henry *et al.*, 2005).

(Alm₅₄₋₅₁Gros₅₂₋₂₃Py₁₁₋₇Spess₁₁₋₂; Supplementary Table 1c; Fig. 4e). Mg-hornblende, actinolitic hornblende, Fe-actinolite and actinolite together with oligoclase-albite, RE-rich epidote and (Ca,F)apatite (Fig. 6e) are also present as the retrogressive assemblage.

In both amphibolite samples, two types of rutile are present: dark-brown, short prismatic crystals (Rt1), from 50–100 μm in length, locally replaced by ilmenite and titanite (Figs. 6f-g) and 2) brick-red, prismatic (Rt2) with aspect ratios between 2 and 3:1, which overgrows titanite and ilmenite (Fig. 6h). In Rt1 from sample MMA1, Zr contents range from 171–2850 ppm, Cr ranges from 13–123 ppm and Nb ranges from 631–922 ppm, while Hf ranges from 5.3–76 ppm. Rt2 from the same sample is characterized by Zr ranging from 173–980 ppm, Cr ranging from 32.8–142.3 ppm, Nb ranging from 660–1720 ppm, while Hf ranges from 7.32–29.1 ppm. Rt1 from sample MMA3 show Zr contents from 155.6–3000 ppm, Cr from 149.2–1970 ppm, Nb from 1180–887 ppm and Hf from 6.48–106 ppm (Supplementary Table 5).

4. b. Pressure–temperature estimations

4. b.1 Bilyipotik Nappe (Ukraine) – metapelites

The modelled metamorphic conditions are based on the whole-rock composition (Table 2) and major rock-forming minerals. Since matrix forming minerals re-equilibrated during the later stages and earlier assemblages could only be inferred from mineral inclusions in refractory phases like garnet, the pressure and temperature estimations here are largely based on the measured garnet compositions in sample SR20c. The modelled garnet compositional isopleths, corresponding to the core composition, define the first metamorphic episode (M1), with a mineral assemblage: Bt + Ph + Msc + Pl + Chl + Grt1 (core) + Ilm + Qtz at 560–630 MPa and 515–535 °C. The modelled isopleths corresponding to garnet rim compositions intercept at much higher pressure and similar temperature of 900–1180 MPa and 590–620 °C with a metamorphic assemblage of Pl + Ph + Msc + Bt + Grt2 (rim) + Rt + Qtz (Fig. 7a), defining the M2 episode. The M1 and M2 episodes mark the prograde metamorphism. Garnet

Table 4. Chemical compositions and crystal-chemical formulae of representative muscovite crystals from metapelites

Sample No	SR20A (UKR)			MMS2 (ROM)			MMS3 (ROM)				
	Component	LoD	Ms1	Ms2	Ms3	Ms1	Ms2	Ms3	Ms1	Ms2	Ms3
SiO ₂	0.04	46.70	46.43	46.14	45.43	45.96	46.30	46.16	46.32	47.29	
TiO ₂	0.04	0.43	0.33	0.37	0.53	0.54	0.66	0.37	0.57	0.28	
Al ₂ O ₃	0.03	36.83	36.97	36.84	34.56	36.24	35.95	35.83	35.49	35.38	
Cr ₂ O ₃	0.01	b.d.l.	b.d.l.	0.13	0.02	0.04	0.04	0.01	b.d.l.	b.d.l.	
FeO	0.10	0.67	0.70	0.75	3.38	0.82	0.74	1.43	1.42	1.78	
MgO	0.02	0.47	0.38	0.45	0.66	0.57	0.60	0.91	0.89	0.44	
MnO	0.08	b.d.l.	b.d.l.	b.d.l.	b.d.l.	b.d.l.	b.d.l.	0.11	b.d.l.	0.08	
Na ₂ O	0.04	2.27	2.12	1.47	0.46	1.60	1.55	0.86	0.85	0.90	
K ₂ O	0.04	8.37	8.63	8.62	10.45	9.21	9.35	9.83	9.86	9.93	
BaO	0.07	0.26	0.21	0.18	b.d.l.	0.40	0.34	0.07	0.13	b.d.l.	
Total		96.00	95.77	94.95	95.49	95.38	95.53	95.58	95.53	96.08	
Crystal-chemical formulae recalculated for 22 O ²⁻											
Si		6.114	6.097	6.100	6.130	6.101	6.140	6.116	6.142	6.163	
Al ^{iv}		1.886	1.903	1.900	1.870	1.899	1.860	1.884	1.858	1.837	
Al ^{vi}		3.796	3.818	3.840	3.626	3.770	3.758	3.711	3.688	3.750	
Ti		0.042	0.033	0.036	0.051	0.054	0.066	0.037	0.057	0.027	
Cr		–	–	0.014	0.000	0.004	0.003	0.001	–	–	
Fe		0.074	0.077	0.083	0.381	0.091	0.082	0.159	0.157	0.194	
Mg		0.091	0.075	0.089	0.134	0.113	0.118	0.179	0.175	0.086	
Mn		–	–	–	0.008	–	–	0.012	–	0.009	
Na		0.576	0.540	0.376	0.121	0.412	0.397	0.221	0.218	0.226	
K		1.397	1.445	1.453	1.858	1.492	1.522	1.762	1.707	1.751	
Ba		0.013	0.011	0.009	0.003	0.021	0.017	0.004	0.007	–	
#mg		0.551	0.493	0.517	0.260	0.553	0.590	0.530	0.527	0.307	

Abbreviations: b.d.l. – below detection limit; #mg = Mg/(Mg+Fe).

isopleths corresponding to composition of the small, elongated post-kinematic garnets (Grt3), intercept at P-T conditions of 500–690 MPa and 550–610 °C, within staurolite field, with an assemblage of Grt + Pl + Msc + Bt + St + Ilm + Qtz (defining the M3 episode; Fig. 7a). Alternatively, staurolite porphyroblasts can be interpreted as a part of peak assemblage. However, the presence of ilmenite inclusions in staurolite (Fig. 3c) suggests that this mineral grew during uplift. These temperature estimates are in agreement with the Henry *et al.* (2005) Ti-in-biotite geothermometry, yielding temperatures of 576–581 °C (Table 2; Fig. 7a). As biotite is stable at all computed P-T conditions, most probably it re-equilibrated throughout the P-T loop. Rare allanite + apatite + carbonate coronas around monazite in metapelites (Fig. 5h) mark retrogression and oxidized fluid influx (M4; Fig. 7a). Chlorite geothermometry (Cathelineau & Nieva, 1985; Jowett, 1991; Kranidiotis & MacLean 1987) implies two phases of late chlorite growth – a higher temperature event at 350–400 °C (in agreement with M4 episode) and a subsequent event of low-temperature chlorite crystallization at 245–300 °C (Table 6).

4. b.2. Bilyipotik nappe (Ukraine) – amphibolites

In the amphibolites, P-T conditions of 880–1030 MPa and 573–620 °C for tschermakitic to aluminos-tschermakitic hornblende coexisting with andesine plagioclase and 610–700 MPa and 610–630 °C for magnesio-hornblende and coexisting plagioclase pairs are determined based on amphibole-plagioclase geobarometry (Molina *et al.* 2015), Ti-in-calcium amphibole geothermometry (Liao *et al.* 2021), coupled with the Blundy & Holland (1990) thermobarometer. These P-T constraints are compatible with a clockwise P-T loop for intercalated metapelites, with ilmenite crystallization at the expense of rutile on the exhumation path in the amphibolites. Decreasing temperature on the retrograde path was associated with an increase in oxygen fugacity and titanite crystallization at the expense of ilmenite/rutile in the amphibolites. That is supported by the low-temperature actinolite growth (423–508 °C, based on Ti-in-calcium amphibole geothermometry by Liao *et al.* (2021) at low pressure at c. 340 MPa (Blundy & Holland 1990) (Supplementary Table 4a).

Table 5. Chemical compositions and crystal-chemical formulae of representative ilmenite, rutile and titanite crystals from metapelites and amphibolites

Compound (wt%)	LoD	SR20a		SR 22		MMS 2		MMA 3		
		Rutile	Ilmenite	Ilmenite	Titanite	Rutile	Ilmenite	Rutile	Ilmenite	Titanite
Nb ₂ O ₅	0.05	0.22	b.d.l.	b.d.l.	b.d.l.	0.12	0.05	b.d.l.	0.05	b.d.l.
V ₂ O ₅	0.08	0.45	0.18	0.12	0.17	0.22	b.d.l.	0.13	0.10	0.10
SiO ₂	0.05		b.d.l.	0.25	30.24	0.07	b.d.l.	0.12	b.d.l.	30.25
TiO ₂	0.03	99.48	53.20	52.63	39.28	99.46	53.16	98.74	52.20	38.38
Cr ₂ O ₃	0.05	–	b.d.l.	b.d.l.	b.d.l.	0.09	b.d.l.	b.d.l.	b.d.l.	b.d.l.
Al ₂ O ₃	0.01	–	0.01	b.d.l.	1.28	b.d.l.	b.d.l.	0.02	b.d.l.	1.36
Fe ₂ O ₃	0.07	0.45	–	–	0.78	0.31	–	0.63	–	0.69
FeO	0.10		42.82	42.76	–	–	42.98	–	44.57	–
MgO	0.02	0.02	0.06	0.05	b.d.l.	b.d.l.	0.03	b.d.l.	0.13	b.d.l.
CaO	0.03	–	–	–	28.67	–	–	–	–	28.64
MnO	0.05	–	3.52	3.57	b.d.l.	b.d.l.	3.74	b.d.l.	2.95	0.05
F	0.03	–	–	–	0.18	–	–	–	–	0.24
Total		100.62	99.79	99.38	100.60	100.27	99.96	99.64	100.00	99.71
Nb ⁵⁺		0.001	0.001	–	–	0.001	0.001	–	0.001	–
V ⁵⁺		0.005	0.007	0.005	0.001	0.002	–	0.001	0.004	0.003
Si ⁴⁺		–	–	0.012	0.985	0.001	–	0.002	1.983	0.994
Ti ⁴⁺		0.991	2.012	1.986	0.963	0.992	2.011	0.988	–	0.948
Cr ³⁺		–	–	–	–	0.001	–	–	–	–
Al ³⁺		–	0.001	–	0.049	–	–	–	–	0.054
Fe ³⁺		0.004	–	–	0.029	0.003	–	0.006	–	0.026
Fe ²⁺		–	1.800	1.798	–	–	1.808	–	1.883	–
Mg ²⁺		0.001	0.004	0.003	–	–	0.002	–	0.009	–
Ca ²⁺		–	–	–	1.001	–	–	–	–	1.008
Mn ²⁺		–	0.150	0.152	–	–	0.159	–	0.126	0.001
F					0.023	–	–	–	–	0.030

4. b.3. Bretila group, vaser infrabuconian nappe (Romania) – metapelites

Similarly to sample SR 20c, sample MMS3 thermodynamic modelling was based on the whole-rock composition (Table 2), garnet compositional zoning patterns and rock-forming mineral assemblages. The modelled Grt isopleths show a prograde path from 455–620 MPa and 545–555 °C through 670–745 MPa and 540–560 °C (M1 - M2 - Grt core) to 910–965 MPa and 645–660 °C (M3 - Grt rim; Fig. 7b). The modelled assemblages change from Grt + Msc + Pl + Bt + St + Ilm + Qtz (M1) to Grt + Msc + Pl + Bt + Rt (M2) and Grt + Ms + Pl + Bt + Rt + Qtz + melt (M3), describing a clockwise P-T loop of increasing pressure at almost constant temperature, culminating in a low degree of partial melting at the inferred peak temperature (Field 13, Fig. 7b), probably obscured by the retrogression. The inclusions of ilmenite and rutile in garnet core and rim correspond to the modelled P-T path starting in ilmenite field going well into the rutile field. The modelled assemblage M3 corresponds with the matrix assemblage observed in the sample (Assemblage 2, MMS3). Temperature estimates based on the Henry *et al.* (2005) geothermometer show values of 530–580 °C (Table 2) and are interpreted as recording retrogression linked to shearing.

Zr-in-rutile geothermometry in sample MMS2 (Zack *et al.* 2004) yields two temperature ranges: a higher temperature one at 654 °C (R1, mean of 18 analyses) and a lower one at 569 °C (R2, mean of 9 analyses), which can be linked to retrogression in the sample (Supplementary Table 5). Temperature estimates employing Ti-in-biotite geothermometry (Henry *et al.* 2005) are 551–590 °C (Table 2), which correlates with the temperature range of the R2 rutile population and are similar to the MMS3 sample.

4. b.4. Bretila group, Vaser infrabuconian Nappe (Romania) – amphibolites

The lack of unaltered plagioclase precludes the use of Pl-Amph geothermobarometry in the MMA1 amphibolite. However, Ti-in-calcium amphibole thermometry implies a temperature range of 688–640 °C (Supplementary Table 4b), and Zr-in-rutile geothermometry from the same rock sample yields a temperature at 672 °C (mean of 23 analyses). While this is in agreement with peak temperature estimates for the MMS2 schist (670–690 °C), the stability field of rutile at that temperature range is above 1000 MPa. The P-T estimates in amphibolite sample MMA3 for coexisting tschermakitic hornblende and andesine plagioclase are c. 800–840

Table 6. Chemical compositions and crystal-chemical formulae of representative chlorite crystals from metapelites

Component	SR20Ca						SR20Cb			
	#1	#2	#3	#4	#6	#7	#1	#2	#3	#4
SiO ₂ (wt.%)	24.52	24.02	23.79	23.90	23.94	23.99	29.20	28.39	28.40	27.22
TiO ₂	0.08	0.10	0.09	0.08	0.10	0.12	0.82	0.92	0.51	0.16
Al ₂ O ₃	23.19	23.12	23.14	23.24	23.56	23.91	18.20	18.10	18.42	18.31
Fe ₂ O ₃	0.88	0.36	0.24	0.64	0.67	0.91	0.92	0.93	0.57	1.20
FeO	25.68	26.85	26.65	25.91	26.78	25.17	26.73	27.09	29.01	29.12
MnO	0.08	0.07	0.08	0.06	0.07	0.10	0.22	0.13	0.18	0.19
MgO	12.32	12.67	12.85	12.68	12.22	12.67	11.24	10.79	10.78	11.11
CaO	b.d.l.	b.d.l.	b.d.l.	b.d.l.	b.d.l.	0.07	0.12	0.13	0.11	0.09
Na ₂ O	b.d.l.	0.08	0.07	b.d.l.	b.d.l.	b.d.l.	b.d.l.	b.d.l.	0.10	n.d.
K ₂ O	0.28	0.00	0.00	0.00	0.00	0.00	2.63	2.38	1.97	0.42
H ₂ O*	11.21	11.21	11.17	11.14	11.21	11.24	11.44	11.25	11.35	11.08
TOTAL	98.24	98.47	98.07	97.64	98.55	98.17	101.52	100.12	101.40	98.89
Si	5.22	5.13	5.10	5.13	5.11	5.11	6.03	5.97	5.93	5.86
Al ^{IV}	2.78	2.87	2.90	2.87	2.89	2.89	1.97	2.03	2.07	2.14
Al ^{VI}	3.07	2.97	2.96	3.03	3.05	3.12	2.52	2.51	2.52	2.53
Ti	0.01	0.02	0.01	0.01	0.02	0.02	0.13	0.15	0.08	0.03
Fe ³⁺	0.14	0.06	0.04	0.10	0.11	0.15	0.14	0.15	0.09	0.19
Fe ²⁺	4.58	4.80	4.78	4.66	4.78	4.48	4.61	4.76	5.07	5.24
Mn	0.01	0.01	0.01	0.01	0.01	0.02	0.04	0.02	0.03	0.03
Mg	3.91	4.04	4.11	4.06	3.89	4.02	3.46	3.38	3.36	3.56
Ca	–	–	–	–	–	0.02	0.03	0.03	0.02	0.02
Na	0.00	0.06	0.05	–	–	–	0.00	0.00	0.08	–
K	0.15	–	–	–	–	–	1.38	1.27	1.05	0.23
OH*	16	16	16	16	16	16	16	16	16	16
Total	35.88	35.95	35.97	35.87	35.86	35.82	36.32	36.27	36.30	35.84
Variety	Ripidolite			Ripidolite			Brunsvigite		Brunsvigite	
Fe/Fe+Mg	0.55	0.55	0.54	0.54	0.56	0.54	0.58	0.59	0.61	0.60
T ₁ [°C]	385	400	404	400	403	404	255	265	271	283
T ₂ [°C]	374	388	393	388	392	393	245	255	261	273
T ₃ [°C]	353	362	365	362	365	364	270	278	282	290

Abbreviations: b.d.l. – below detection limit. Temperature is based on three geothermometers: T1: Cathelineau & Nieva (1985), T2: Jowett (1991), and T3: Kranidiotis & MacLean (1987).

MPa and 748–756 °C, while P-T estimates for coexisting Mg-hornblende and oligoclase yielded 450–500 MPa and 654–670 °C, within the ilmenite stability field. The Zr-in-rutile geothermometer yielded a mean value of 670 °C (Rt2), while a small rutile population (Rt1; 5 grains) yielded a mean temperature of c. 900 °C. As there is no other proof for high-temperature metamorphism in Bretia Group, these results remain uncertain.

The presence of low-grade (retrograde) amphiboles (actinolitic hornblende, Fe-actinolite and actinolite) and oligoclase-albite lie on the cooling path with a pressure of 366–480 MPa and a temperature range 317–619 °C as defined by Ti-in amphibole geothermometry (Liao *et al.* 2021) and Blundy & Holland (1990) thermobarometer (Supplementary Table 4b).

4. c. Geochronology

4. c.1. Monazite geochemistry and dating

Chemical EPMA dating of monazite crystals was undertaken on the metapelite sample SR20C (Bilyipotik Nappe). Chemically homogeneous monazite crystals ranging in size between 15 and 50 µm in size were dated, including inclusions in garnet and in the matrix (Fig. 4a, b). Ce and La are the most abundant REE (23.1–29.5 wt% Ce₂O₃ and 9.7–13.7 wt % La₂O₃), while ThO₂ and UO₂ contents are 1.0–3.1 wt% and 0.5–1.15 wt%, respectively (Supplementary Table 1). On a Th versus Pb plot, two main generations of monazite were distinguished, and only one of them intersects the origin (Fig. 8a–c). Thirty-five point analyses of this population yielded an average age of 351 ± 14 Ma (MSWD = 0.28).

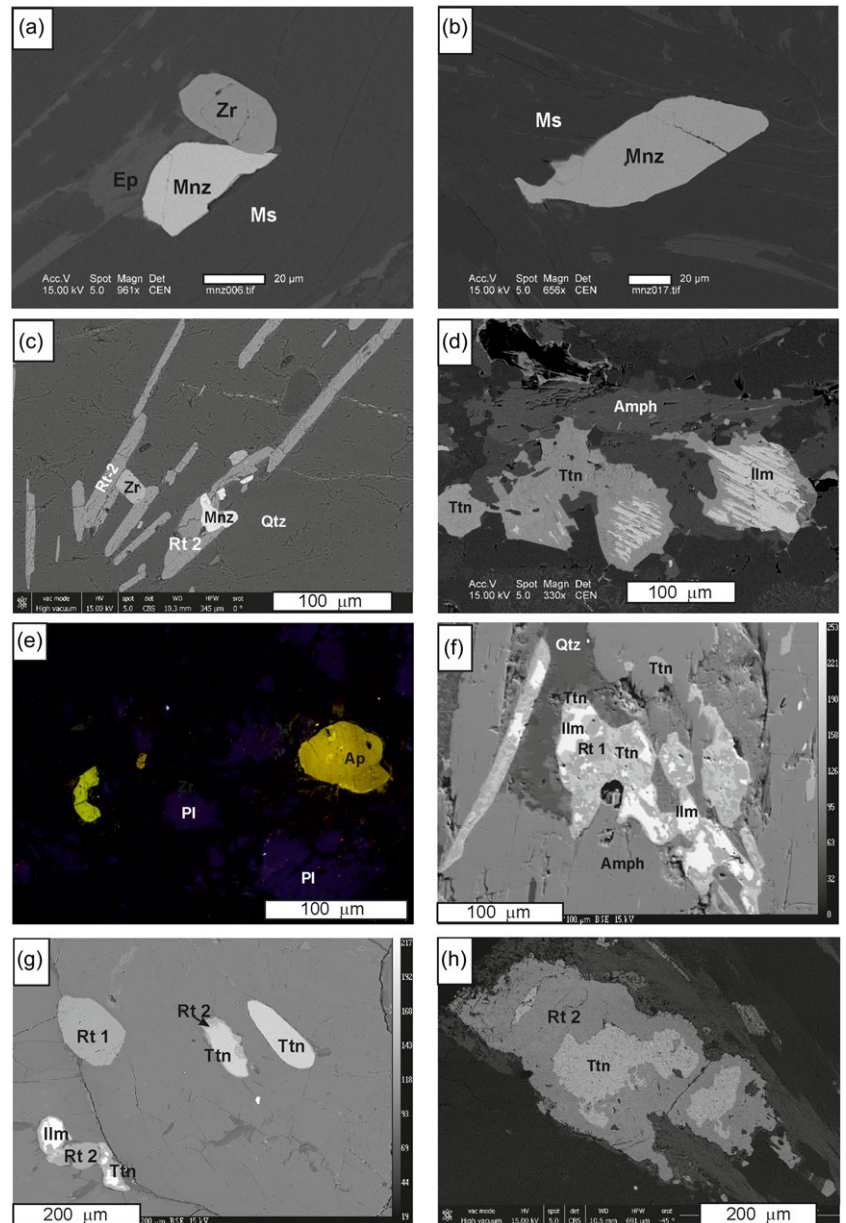


Figure 6. BSE and CL images from metapelites and amphibolites of the Maramuresh Massif (Romania): (a) monazite (Mnz1) (with secondary epidote – Ep) and zircon (Zr) inclusions in quartz from schist sample MMS2; (b) deformed monazite (Mnz1) from the MMS2 schist; (c) aggregates of rutile needles (Rt2), zircon (Zr) and monazite (Mnz) in quartz from the MMS3 schist sample; (d) ilmenite (Ilm) replacement by titanite (Ttn) in amphibolite sample MMA1; (e) CL image of apatite from the MMS3 schist; (f) intergrowths of rutile (Rt) and ilmenite (Ilm), replaced by titanite (Ttn) in amphibolite sample MMA3; (g) associations of the two generations of rutile: primary Rt 1 and secondary Rt 2, locally overgrowing titanite (Ttn) and ilmenite from the MMA1 amphibolite; (h) replacement of titanite by secondary rutile in the MMA3 amphibolite.

Twenty-four point analyses yielded an average age of 287 ± 17 Ma (MSWD = 0.29), two points represent inherited pre-Variscan ages (c. 403 and 422 Ma), one point yielded an age of $70 \text{ Ma} \pm 106$ Ma, two point analyses yielded early Alpine ages (171 and 172 Ma – rims of monazite from matrix biotite) and one point analyses was rejected due to disequilibrium (Supplementary Table 1; Figs. 8a and b).

Fifty-nine (59) chemically homogeneous Ce and La rich monazite crystals from the metapelite sample MMS2 (Bretila Group) were analysed ($\text{La}_2\text{O}_3 = 13.6\text{--}15.7$ wt %, $\text{Ce}_2\text{O}_3 = 27.6\text{--}29.8$ wt %, $\text{ThO}_2 = 7.4\text{--}3.6$ wt % and $\text{UO}_2 = 0.61\text{--}1.06$ wt %). Fifty-seven point analyses yielded an average age of 327.6 ± 8.5 Ma (MSWD = 0.35; Fig. 9a). Two-point analyses that yielded lower U contents ($\text{UO}_2 = 0.45\text{--}0.48$ wt %) yielded ages of 238 Ma and 259 Ma (Supplementary Table 1).

4. c.2. Apatite geochemistry and U-Pb dating Bilyipotik Unit

Short prismatic apatite crystals from the Bilyipotik Nappe, 70–150 μm in length, are fluorapatite in composition. A total of 64 spot

analyses were undertaken on 53 crystals from the SR21 sample, while 86 spot analyses were undertaken on sample SR22. On the support vector machine (SVM) apatite classification diagrams (Sr/Y vs LREE [La, Ce, Pr, Nd]; O’Sullivan *et al.* 2020) the apatite analyses from the SR21 and SR22 amphibolites plot in low- and medium-grade metamorphic (LM) and I-type granitoids and mafic igneous (IM) fields. Two analyses from the SR21 amphibolite plot in the high-grade metamorphic (HM) field (Fig. 10). Th/U ranges from 0.003–1.402 in SR21 to from 0.012–2.322 in SR22 sample, while Sr/Mn is mostly above 0.5 (Supplementary Table 6). Despite the small differences in chemistry, apatite from both samples yielded very similar U-Pb ages. Excluding one core, the 52 grains of metamorphic apatite from SR 21 sample yielded a Tera-Wasserburg lower intercept age of 317.3 ± 5.5 Ma (MSWD = 2.3; Fig. 8d), while all 86 analyses from the SR22 sample yielded a Tera-Wasserburg lower intercept age of 319.0 ± 2.5 Ma (MSWD = 0.88; Fig 8e; Supplementary Table 6).

Bretila Unit

Thirteen short prismatic fluorapatite crystals (50–100 μm in length) from the MMA1 amphibolite were analysed, yielding a

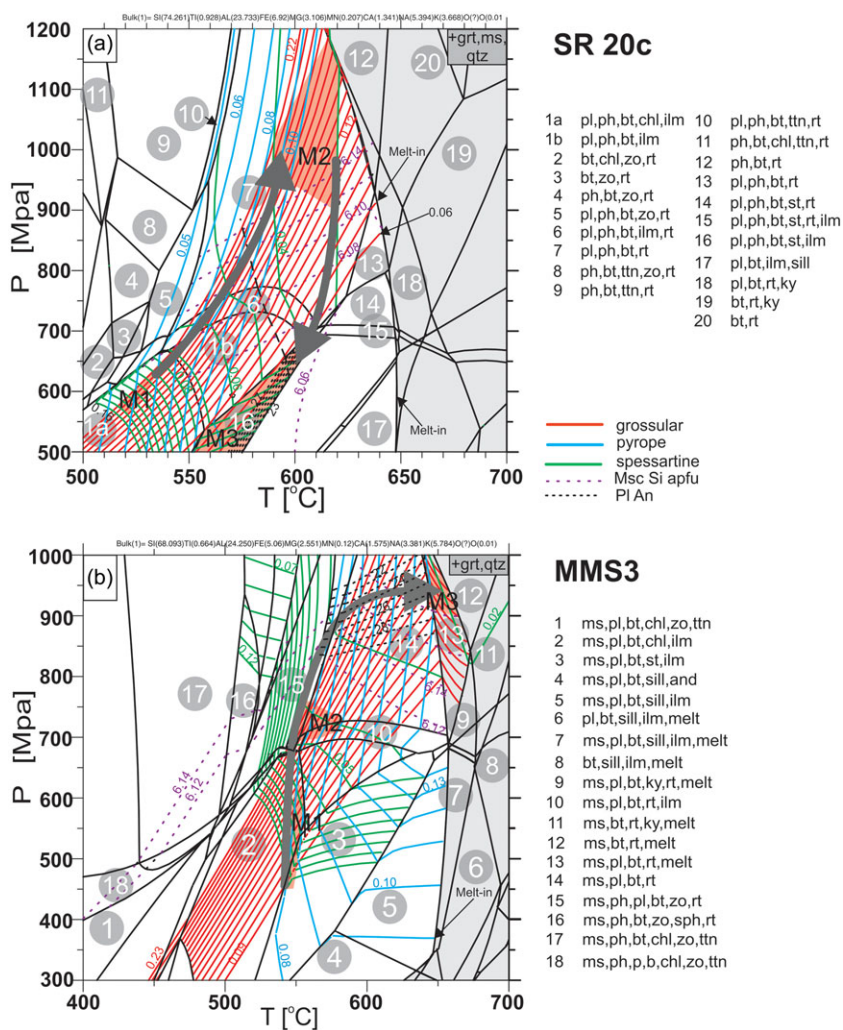


Figure 7. P-T paths of the metamorphic evolution of the two metapelite rocks from the Marmarosh/Maramuresh Massif with the stability fields of the main mineral assemblages indicated. (a) Ukrainian part; (b) Romanian part. See the main text for explanations. Abbreviations according to Whitney & Evans (2010) are amph – amphibole, bt – biotite, chl – chlorite, grt – garnet, ky – kyanite; pl – plagioclase, kf – K-feldspar, ms – muscovite, ph – phengite, qtz – quartz, rt – rutile, sill – sillimanite, ilm – ilmenite, ttn – titanite; st – staurolite, zo – zoisite.

Tera-Wasserburg lower intercept age of 280.6 ± 32 Ma (MSWD = 0.71; Fig 9b; Supplementary Table 5). On the SVM apatite classification diagrams (Sr/Y vs LREE [La, Ce, Pr, Nd]; O’Sullivan *et al.* 2020), the apatites plot in the low- and medium-grade metamorphic (LM) and high-grade metamorphic (HM) fields (Fig. 10). The Sr/Mn and Sr/Y ratios are below 0.5 and 1, respectively (Supplementary Table 6).

Forty-eight short-prismatic fluorapatite crystals from the amphibolite sample MMA3 (60–120 μm in length) were analysed. All points plot exclusively in the LM field on the SVM apatite classification diagram (Fig. 10) (O’Sullivan *et al.* 2020), yielding a Sr/Mn ratio above 0.5 and a Tera-Wasserburg lower intercept age of 280.8 ± 27 Ma (MSWD = 0.41; Fig. 9c; Supplementary Table 5).

4. c.3. Titanite geochemistry and U-Pb dating (Bretila group)

Ten elongated titanite crystals from the amphibolite sample MMA3 (70–110 μm in length) were analysed. The aluminium content ranges from 6220–15390 ppm, yttrium ranges from 72.5–1220 ppm and correlates positively with ΣREE , ranging from 51.37–2297.40 ppm ($r^2 = 0.935$). Uranium prevails over thorium ($\text{Th}/\text{U} = 0.09\text{--}0.22$; Supplementary Table 5). All ten analyses yielded an imprecise Tera Wasserburg age of 322 ± 25 Ma (MSWD = 4.0; Fig. 9d; Supplementary Table 5).

4. c.4. Rutile geochemistry and U-Pb dating (Bretila group)

In both amphibolite samples, two populations of rutile were analysed: Rt1 and Rt2. In sample MMA1 25, spot analyses on 35 crystals of first-generation rutile (Rt1) were undertaken. They yielded a Tera-Wasserburg lower-intercept age of 341 ± 18 Ma (MSWD = 1.45; Fig. 9e; Supplementary Table 5). Twenty-eight brick-red and elongated rutile crystals (Rt 2) were analysed. They yielded a lower intercept age of 276 ± 15 Ma (MSWD = 2.3; Fig. 9f; Supplementary Table 5).

Five short prismatic grains of rutile from amphibolite MMA3 yielded a Tera Wasserburg lower intercept age of 354 ± 21 Ma (MSWD = 0.55; Fig. 9g; Supplementary Table 5).

Twenty-seven dark-red and prismatic rutile crystals from the metapelite sample MMS2, ranging from 80 to 200 μm in length, were selected for analysis. From these crystals, 21 yielded a Tera Wasserburg lower intercept age of 278 ± 14 Ma (MSWD = 2.2; Fig. 9h; Supplementary Table 5), while six analyses do not lie on the discordia intercept.

5. Discussion

5. a. Linking the P-T paths with geochronology

5. a.1. Bilyipotik Nappe (Ukraine)

Monazite is thermally resistant mineral, with a Pb closure temperature exceeding 900 °C (Crowley & Ghent, 1999; Cherniak *et al.* 2004), but it

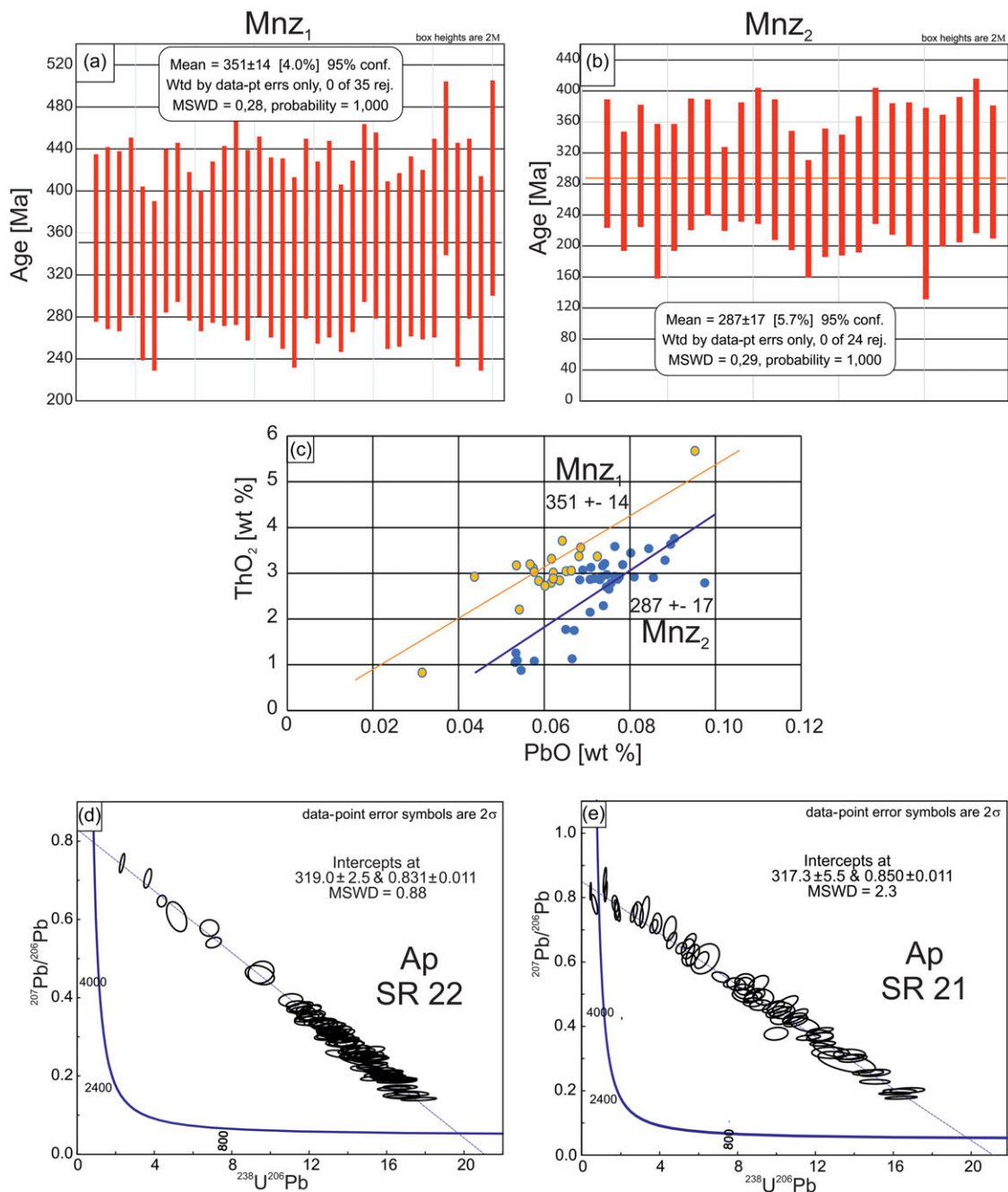


Figure 8. Geochronology of metamorphic rocks from the Marmorosch Massif (Ukraine): (a) and (b) weighted mean CHIME age of monazite Mnz 1 and Mnz 2 from sample SR20C; (c) ThO₂ vs PbO plot showing two populations of monazite in the SR20C schist; (d) and (e) U-Pb LA-ICP-MS Tera-Wasserburg apatite concordias.

can crystallize over a wide range of temperatures and in magmatic, metamorphic and hydrothermal environments (Spear, 2010). The older monazite (Mz1), found as inclusions in garnets (both in the cores and rims), yields an age of 351 ± 14 Ma (Fig. 8a) and constrains garnet crystallization to Meso-Variscan M1 – M2 metamorphism (Figs. 7a; 10a). The presence of rutile, intergrown with ilmenite, shows out that the sample passed through the stability fields of both phases during the metamorphic evolution of the rock complex (Fig. 11a).

The younger, second-generation monazite (Mz2; 287 ± 17 Ma – M4 episode; Figs. 8b, 11a) can be linked to post-Variscan (Permian) shearing, either within the monazite stability field or at the transition between the monazite and allanite stability fields

on the retrograde path. Small monazite crystals, locally overgrown by allanite – REE-epidote coronas, imply oxidized fluid ingress, below 400–450 °C and c. 400 MPa (Finger *et al.* 1998) and are linked to the higher temperature chlorite population crystallizing at temperatures of 350–400 °C (M5; Fig. 11a). This episode was, however, intensive enough to partially mobilize Pb in monazite, which would explaining why PbO *versus* ThO₂ line does not meet the origin on a Th versus Pb plot (Fig. 8c).

Apatite has a lower closure temperature window for the U-Pb system (350–550 °C, Schoene & Bowring, 2007) and yields reasonably precise age data (317.3 ± 5.5 Ma and 319.0 ± 2.5 Ma for the M3 episode; Fig. 11a), which constrains the history of the

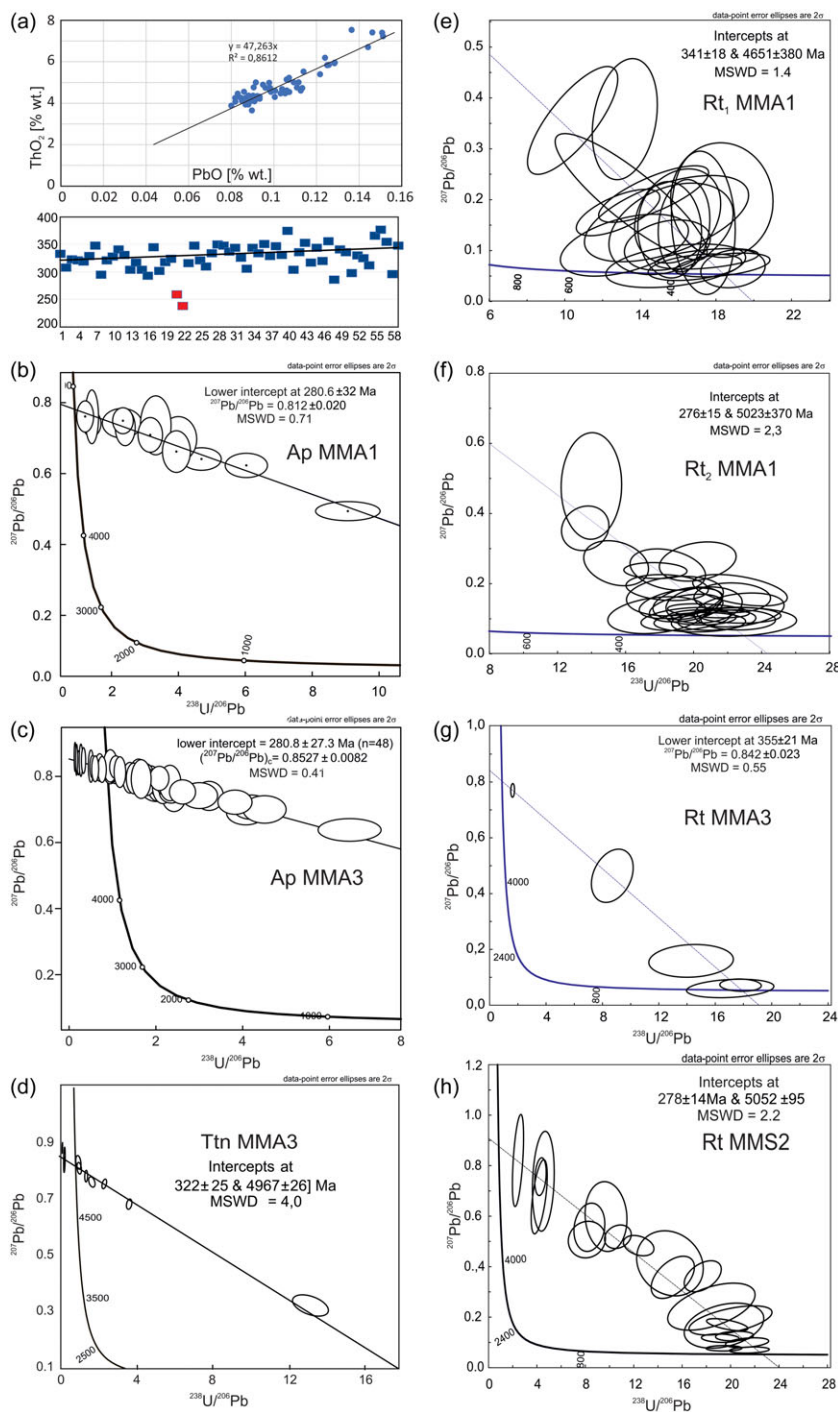


Figure 9. Geochronology of metamorphic rocks from the Maramuresh Massif (Romania): (a) ThO₂ vs PbO plot and weighted mean CHIME age of monazite Mnz 1 from the MMS3 schist sample; b-h) U-Pb LA-ICP-MS Tera-Wasserburg concordias for apatite, titanite and two rutile generations from amphibolites and metapelites.

cooling path (Chew & Spikings, 2015; Chew *et al.* 2011). The apatite affinity on the SVM biplot suggests hydrothermal/low-grade metamorphic resetting of mafic igneous apatite (particularly Sr/Mn ratios) that underwent high-grade (amphibolite facies) metamorphism (Fig. 10). As shown by the replacement of intergrown ilmenite and rutile by titanite in the amphibolites, oxidizing conditions are again inferred for the M4 episode (Fig. 11a). A few rims of actinolite/ actinolitic hornblende yielded temperatures of 423 °C, 481 °C and 508 °C, with pressures at 340 MPa and below (Supplementary Table 4a), all located below the closure temperature of apatite, supporting the retrogression path described above (Fig. 11a).

5. a.2. Bretila group (Romania)

Four U-Pb mineral system pairs were used to date the metamorphic episodes. The oldest (Variscan) episode was defined by the Rt1 population from the MMA1 and MMA3 amphibolites and yielded Tera-Wasserburg U-Pb lower intercept ages of 341 ± 18 Ma and 354 ± 21 Ma, respectively (Figs. 9e, g; Supplementary Table 6) and defining the prograde mineral assemblage (M1 – M2 metamorphic episodes; Fig. 11b). These ages overlap with the U-Th-Pb ages of texturally early monazite from the Bilyipotik Nappe, Ukraine (Fig. 8a).

Titanite from the MMA3 amphibolite yielded an imprecise Tera-Wasserburg U-Pb lower intercept age of c. 322 Ma, in

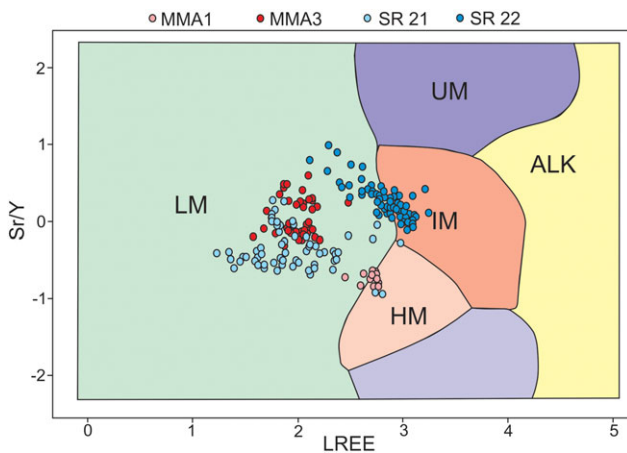


Figure 10. Trace element geochemistry of apatite from the amphibolite samples on a support vector machine (SVM) classification diagrams (Sr/Y vs LREE [La, Ce, Pr, Nd]) after O'Sullivan *et al.* (2020). ALK = alkaline-rich igneous; HM = high-grade metamorphic; IM = I-type granitoids and mafic igneous; LM = low- and medium-grade metamorphic; S = S-type granites; UM = ultramafic igneous.

agreement with the U-Th-Pb monazite CHIME age of 327.6 ± 8.5 Ma (Figs. 9a & 9d) from the interleaved metapelite sample MMS2, possibly marking cooling into the titanite stability field (M4) and slightly older than the U-Pb apatite ages of c. 317 and 319 Ma from the Bilyipotik Nappe.

The Rt2 rutile from the MMS2 schist sample yielded a Tera-Wasserburg lower intercept age of 278 ± 14 Ma; Fig. 9h). Low-temperature Rt2 rutile, replacing titanite in the MMA1 amphibolite sample (Fig. 9f) yielded a similar Tera-Wasserburg lower intercept age of 278 ± 14 (Fig. 9f), in agreement with an imprecise apatite Tera-Wasserburg lower intercept age of 280.6 ± 32 Ma from the same sample (Fig. 9b). A similar Tera-Wasserburg age of 280.8 ± 27 Ma was determined from the MMA3 amphibolite sample, with these c. 280 Ma ages marking M5 shearing and retrogression (Fig. 11b). The apatite crystals from the MMA1 amphibolite plot mostly in HM field (Fig. 10) and yielded the lowest Sr/Mn and Sr/Y ratios, atypical of a metabasite protolith (Supplementary Table 6). The MMA3 amphibolite apatite plot mostly in LM field (Fig. 10) with Sr/Mn and Sr/Y ratios mainly below 0.5 and 1, respectively. In both amphibolite samples fluid-assisted recrystallization of apatite crystals is assumed to take place during low-grade metamorphism, likely related to shearing. This is in agreement with the presence of late, post-kinematic Mg-hornblende and secondary actinolite-group minerals, that crystallized in a P-T range of 366–428 MPa and 525–620 °C (Mg-hbl and Act-Hbl) and 317–456 °C (Supplementary Table 4b; Fig. 11b). As in the case of the Bilyi Potik suite, these P-T estimates can be related to titanite and apatite/Rt2 growth and mark the retrogression path related to decompression and shearing. In the entire massif, late muscovite is post-kinematic, with low phengite contents and represents low pressure (< 200 MPa) retrogression (M6 in Ukraine – Fig. 11a and M5 in Romania – Fig. 11b).

5. b. Geodynamic context and P-T-t evolution

The Marmarosh/Maramuresh Massif is interpreted as a fragment of the Paleozoic North European Platform that rifted off in the Mesozoic (Schmid *et al.* 2008; Matenco *et al.* 2010). A Laurussian affinity for the massifs is supported by the presence of Caledonian

volcanic arc rocks, likely representing the eastern branch of the European Caledonides (Munteanu & Tatu 2003; Gawęda *et al.* 2022).

The P-T-t data, reported here, place the Bilyipotik/Infrabucovinian nappes of the Marmarosh/Maramuresh Massif within the European Variscides. They were subjected to epidote-amphibolite to amphibolite facies Mid-Variscan (c. 350 Ma) metamorphism (M1 – M2 in Romania or M1 – M4 in Ukraine). In the northern part (Bilyipotik Nappe), the pressure increase to 900–1200 MPa (M3; Fig. 11a) can be interpreted as a result of nappe stacking. In the Infrabucovinian Nappes (Bretila Group) to the south, the maximum pressure did not exceed 1000 MPa (Figs. 11a, b). The Bilyipotik Variscan nappe was likely structurally deeper during Variscan nappe stacking. Based on an assumed westward vergence of the pre-Alpine thrusts Săndulescu (1984) and Krautner & Bindea (2002) considered that the Bretila Group of the Infrabucovinian Nappes was the structurally highest of pre-Alpine (i.e. Variscan) units, which also supports the lowermost position of the northern (Ukrainian) Bilyipotik nappe. A similar Variscan P-T scenario has been documented in the West Sudetes (Leszczyniec Complex) and is interpreted as recording the transition from oceanic to continental subduction following consumption of the Saxoturingian Ocean (Młynarska *et al.* 2024). The similarity in age and P-T conditions of peak metamorphism represents another link between Eastern Carpathian pre-Alpine basement with the Central European Variscides.

Peak metamorphism in the Marmarosh/Maramuresh Massif is followed by Late Carboniferous exhumation and shearing at c. 317–330 Ma (Figs. 11a, b). Post-Variscan shearing in the Central European Variscides was likely related to orogen-parallel extension and exhumation of basement blocks (Franke, 2014 and references therein; Franke & Stein, 2000; Franke & Żelaźniewicz, 2023). This Permian shearing event is more pronounced in the southern (Romanian) parts of the massif, with a c. 280–290 Ma event recorded by U-Pb apatite and rutile ages (second-generation rutile) and supported by the petrological evidence for retrogression both in metapelites and amphibolites. To the south, Permian and later retrogression is found in the Rodna Nappe (Figs 1c & 2b) (Ar-Ar ages of 200–280 Ma; Culshaw *et al.* 2012) interpreted as post-Variscan – pre-Alpine rifting (future Penninic Ocean; Plašienka, 2012 and references therein). Permian tectonism (c. 260–275 Ma) has also been documented in the Central Western Carpathians both by chemical monazite dating and U-Pb apatite dating (Finger *et al.* 2003; Gawęda *et al.* 2018) and is associated with extensional tectonics and a high mantle heat flux (Broška & Uher, 2001; Finger *et al.* 2003 and references therein).

The P-T conditions of the Marmarosh/Maramuresh Massif are therefore similar to the pre-Mesozoic crystalline basement of the Alps (Schulz, 2021), recording the same Variscan and post-Variscan collision-related crustal thickening, exhumation and Permian shearing. The principal difference is the lack of Mesozoic Variscan granitoids and HP/HT rocks in the Marmarosh/Maramuresh Massif, that is typical of the pre-Mesozoic basement of the Alps (von Raumer *et al.* 2013 and references therein). The metamorphic basement of the Marmarosh/Maramuresh Massif thus likely formed part of the external zone of Variscan orogen, most probably overthrust onto the Baltica/Laurussia margin (see Mazur *et al.* 2020 for discussion). The pre-Alpine crystalline fragments/massifs of the Alps and Outer Carpathians likely represent the same microcontinent, dismembered during Alpine orogenesis.

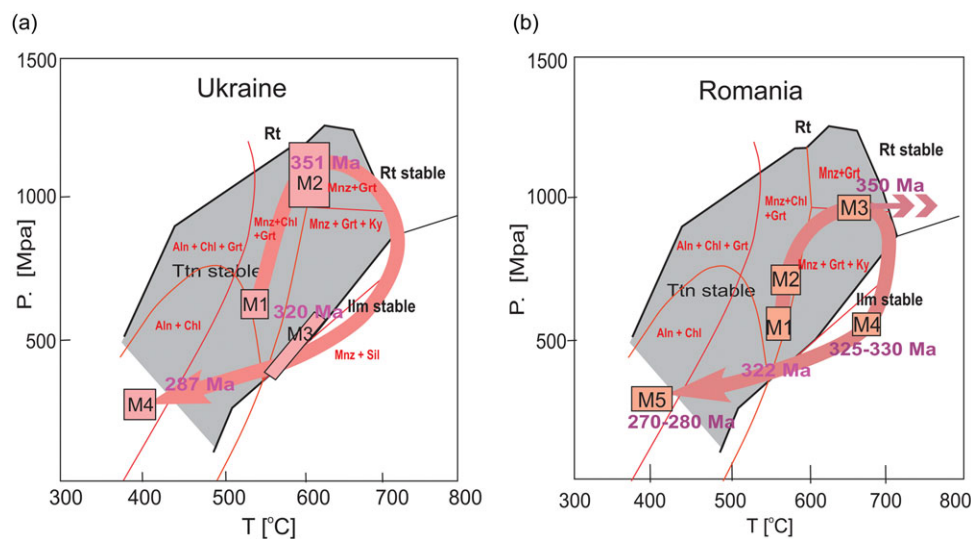


Figure 11. A synthesis of the metamorphic paths from the northern (Ukrainian) (a) and southern (Romanian) (b) parts of the Marmarosh/Maramuresh Massif. See the main text for explanations. Red stability fields after Spear (2010).

6. Conclusions

1. Metapelite-amphibolite successions from the Marmarosh/Maramuresh Massif show similar P-T-t histories as shown by U-Th-Pb dating of monazite, apatite, rutile and titanite and P-T modelling and enables detailed correlation between the northern Bilyipotik Nappe (Ukraine) and the southern Bretila Group (Romania).

2. The peak of prograde metamorphism is dated at c. 350 Ma and records Meso-Variscan nappe stacking during accretion to Laurussia. The P-T conditions of Meso-Variscan metamorphism vary between 900–1180 MPa and 515–535 °C for the Bilyipotik Nappe in the north and 910–965 MPa and 645–660 °C for the Bretila Group in the south.

3. Retrogression during late-Variscan (c. 317 Ma–330 Ma) to post-Variscan (c. 280–290 Ma) times was associated with shearing, likely linked to extension predating the opening of the Penninic Ocean.

4. These data allow linking of the Marmarosh/Maramuresh Massif to the Central European Variscides, with the Marmarosh/Maramuresh likely representing the external zone of the Variscan orogen. We infer that all crystalline, Pre-Mesozoic fragments in the Alps and Carpathians represent the remnants of the same microcontinent, dismembered during Alpine orogenesis.

Supplementary material. supplementary material for this article can be found at <https://doi.org/10.1017/S0016756824000542>

Acknowledgements. This study was financially supported by the internal University of Silesia project entitled: Linking East with the West – geological history of the Marmarosh/Maramuresh Massif (Ukraine/Romania) given to A.G. D.C. acknowledges past and present support from Science Foundation Ireland (SFI) through research grants 12/IP/1663, 13/RC/2092 and 13/RC/2092_P2 (iCRAG Research Centre) and 15/IA/3024. iCRAG is funded under the SFI Research Centres Programme. Detailed comments of the editor Dr Simon Schorn, reviewer Alexandre Peillod and an anonymous reviewer led to a clearer presentation of the paper and are gratefully acknowledged.

Competing interests. The authors declare none.

References

Aleinikoff JN, Wintsch RP, Fanning CM and Dorais MJ (2002) U–Pb geochronology of zircon and polygenetic titanite from the Glastonbury

complex, Connecticut, USA: an integrated SEM, EMPA, TIMS, and SHRIMP study. *Chemical Geology* **188**, 125–147.

Balintoni I and Balica C (2013) Carpathian peri-Gondwanan terranes in the East Carpathians (Romania): a testimony of an Ordovician, North-African orogeny. *Gondwana Research* **23**, 1053–1070.

Blundy JD and Holland TJB (1990) Calcic amphibole equilibria and a new amphibole-plagioclase geothermometer. *Contribution to Mineralogy and Petrology* **104**, 208–244.

Bónová K, Bóna J, Pańczyk M, Kováčik M, Mikuš T and Laurinc D (2019) Origin of deep-sea clastics of the Magura basin (Eocene Makovica sandstones in the outer Western Carpathians) with constraints of framework petrography, heavy mineral analysis and zircon geochronology. *Palaeogeography, Palaeoclimatology, Palaeoecology* **514**, 768–784.

Broska I and Uher P (2001) Whole-rock chemistry and genetic typology of West Carpathians Variscan granitoids. *Geologica Carpathica* **52**, 79–90.

de Capitani C and Brown TH (1987) The computation of chemical equilibrium in complex systems containing non-ideal solutions. *Geochimica et Cosmochimica Acta* **51**, 2639–2652.

de Capitani C and Petrakakis K (2010) The computation of equilibrium assemblage diagrams with Theriak/Domino software. *American Mineralogist* **95**, 1006–1016.

Cathelineau M and Nieva D (1985) A chlorite solid solution geothermometer. The Los Azufres (Mexico) geothermal system. *Contribution to Mineralogy and Petrology* **91**, 235–244.

Cherniak DJ, Watson EB, Grove M, Harrison TM (2004) Pb diffusion in monazite: A combined RBS/SIMS study. *Geochimica et Cosmochimica Acta* **68**(4), 829–840.

Chew DM, Sylvester PJ and Tubrett MN (2011) U–Pb and Th–Pb dating of apatite by LA–ICP–MS. *Chemical Geology* **280**, 200–216.

Chew DM, Petrus JA & Kamber BS (2014) U–Pb LA–ICPMS dating using accessory mineral standards with variable common Pb. *Chemical Geology* **363**, 185–199.

Chew DM and Spikings R (2015) Geochronology and thermochronology using apatite: time and temperature, lower crust to surface. *Elements* **11**(3), 189–194.

Chew D, Babechuk MG, Cogne M, Mark C, O’Sullivan GJ, Henrichs IA, Doepke D and McKenna CA (2016) (LA,Q)–ICPMS trace element analyses of Durango and McClure mountain apatite and implications for making natural LA–ICPMS mineral standard. *Chemical Geology* **435**, 35–48.

Cochrane R, Spikings RA, Chew D, Wotslaw J-F, Chiaradia M, Tyrell S, Schaltegger U and Van der Lelij R (2014) High temperature (>350 °C) thermochronology and mechanisms of Pb loss in apatite. *Geochimica et Cosmochimica Acta* **127**, 39–56.

Coggon R and Holland TJB (2002) Mixing properties of phengitic micas and revised garnet–phengite thermobarometers. *Journal of Metamorphic Geology* **20**, 683–696.

- Crowley JL and Ghent ED** (1999) An electron microprobe study of the U–Th–Pb systematics of metamorphosed monazite: the role of Pb diffusion versus overgrowth and recrystallization. *Chemical Geology* **157**, 285–302.
- Culshaw N, Mosonyi E and Reynolds P** (2012) New ⁴⁰Ar/³⁹Ar laser single-grain ages of muscovites from mylonitic schists in the Rodna Mountains, Eastern Carpathians, Romania: correlations with microstructure. *International Journal of Earth Sciences* **101**, 291–306.
- Finger F, Broska I, Roberts MP, Schermaier A** (1998) Replacement of primary monazite by apatite-allanite-epidote coronas in an amphibolite facies granite gneiss from the Eastern Alps. *American Mineralogist* **98**, 248–258.
- Finger F., Broska I, Haunschmid B, Hrasko L, Kohut M, Krenn E, Petrik I, Riegler G and Uher P** (2003) Electron-microprobe dating of monazites from Western Carpathian basement granitoids: plutonic evidence for an important Permian rifting event subsequent to Variscan crustal anatexis. *International Journal of Earth Sciences* **92**, 86–98.
- Franke W, Dallmeyer RD, Weber K** (1995) Geodynamic evolution. In *Pre-Permian geology of Central and Western Europe* (eds D Dallmeyer, W Franke, K Weber) pp. 579–593. Berlin: Springer..
- Franke W** (2014) Topography of the Variscan orogen in Europe: failed–not collapsed. *International Journal of Earth Sciences* **103**, 1471–1499.
- Franke W and Stein E** (2000) Exhumation of high-grade rocks in the Saxo-Thuringian Belt: geological constraints and geodynamic concepts. In *Orogenic processes: quantification and modelling in the Variscan Belt* (eds W Franke, V Haak, O Oncken, D Tanner), pp. 337–354. Geological Society of London, Special Publication no.179.
- Franke W and Żelaźniewicz A** (2023) Variscan evolution of the Bohemian Massif (Central Europe): Fiction, facts and problems. *Gondwana Research* **124**, 351–377.
- Gawęda A, Szopa K, Chew D, O’Sullivan GJ, Burda J, Klötzli U and Golonka J** (2018) Variscan post-collisional cooling and uplift of the Tatra Mountains crystalline block constrained by integrated zircon, apatite and titanite LA-(MC)-ICP-MS U-Pb dating and rare earth element analyses. *Chemical Geology* **484**, 191–209.
- Gawęda A, Golonka J, Waškowska A, Szopa K, Chew D, Starzec K and Wieczorek A** (2019) Neoproterozoic crystalline exotic clasts in the polish outer Carpathian flysch – remnants of the Proto-Carpathian continent? *International Journal of Earth Sciences* **108**, 1409–1427.
- Gawęda A, Szopa K, Golonka J, Chew D, Stepanyiuk L, Belskyy V, Waškowska A, Siliuskas L and Drakou F** (2022) Collision with Gondwana or with Baltica? Ordovician magmatic arc volcanism in the Marmarosh Massif (Eastern Carpathians, Ukraine). *International Journal of Earth Sciences* **111**, 2181–2198.
- Golonka J, Gahagan L, Krobicki M, Marko F, Oszczytko N and Ślęczka A** (2006) Plate tectonic evolution and paleogeography of the circum-carpathian region. In *The Carpathians and their Foreland: Geology and hydrocarbon resources* (eds J. Golonka and F. Picha), pp. 11–46. American Association of Petroleum Geologists Memoir no. 84.
- Golonka J, Gawęda A and Waškowska A** (2021) Carpathians. In *Encyclopedia of Geology 2nd Edition* (eds D. Alderson & S.A. Elias SA), pp 372–381. Elsevier, Amsterdam, The Netherlands. <https://doi.org/10.1016/B978-0-12-409548-9.12384-X>.
- Green ECR, White RW, Diener JFA, Powell R, Holland TJB and Palin RM** (2016) Activity-composition relations for the calculation of partial melting equilibria in metabasic rocks. *Journal of Metamorphic Geology* **34**, 845–869.
- Henry DJ, Guidotti CV and Thomson JA** (2005) The Ti-saturation surface for low-to-medium pressure metapelitic biotites: Implications for geothermometry and Ti substitution mechanism. *American Mineralogist* **90**, 316–328.
- Holland T and Powell R** (2003) Activity-composition relations for phases in petrological calculations: an asymmetric multicomponent formulation. *Contributions to Mineralogy and Petrology* **145**, 492–501
- Holland TJB and Powell R** (2011) An improved and extended internally consistent thermodynamic dataset for phases of petrological interest, involving a new equation of state for solids. *Journal of Metamorphic Geology* **29**, 333–383.
- Jowett E** (1991) Fitting iron and magnesium into the hydrothermal chlorite geothermometer. In Abstract Book. In: *Proceedings of the GAC/MAC/SEG Joint Annual Meeting*, Toronto, Canada 16, A62.
- Kennedy A.K, Kamo SL, Nasdala L and Timms NE** (2010) Grenville skarn titanite: potential reference material for SIMS U-Th-Pb analysis. *Canadian Mineralogist* **48**, 1423–1443.
- Kranidiotis P and MacLean WH** (1987) Systematics of chlorite alteration at the Phelps Dodge massive sulfide deposit, Matagami, Quebec. *Economical Geology* **82**, 1898–1911.
- Krätner HG** (1988) East Carpathians. In *Precambrian in younger Fold Belts* (ed V. Zoubek), pp. 625–63. J. Wiley, London.
- Krätner HG and Bindea G** (2002) Structural units in the pre-Alpine basement of the Eastern Carpathians. *Geologica Carpathica* **53**, 143–146.
- Krestianinov E, Amelin Y, Neymark LA and Aleinikoff JN** (2021) U-Pb systematics of uranium-rich apatite from Adirondacks: inferences about regional geological and geochemical evolution, and evaluation of apatite reference materials for in situ dating. *Chemical Geology* **581**, 120417. <https://doi.org/10.1016/j.chemgeo.2021.120417>.
- Leake BE, Wooley AR, Birch WD, Burke EAJ, Ferraris G, Grice JD, Hawthorne FC, Kisch HJ, Krivovichev VG, Schumacher JC, Stephenson NCN and Whittaker EJW** (2004) Nomenclature of amphiboles: additions and revisions to the international mineralogical association’s amphibole nomenclature. *American Mineralogist* **89**, 883–887.
- Liao Y, Wei C and Rehman HU** (2021) Titanium in calcium amphibole: Behavior and thermometry. *American Mineralogist* **106**, 180–191.
- Liu Z-C, Wu F-Y, Yang Y-H and Wilde SA** (2012) Neodymium isotopic compositions of the standard monazites used in U - Th - Pb geochronology. *Chemical Geology* **334**, 221–239.
- Ludwig KR** (2012) Isoplot/Ex, v. 3.75. Berkeley Geochronology Center Special Publication, 5.
- Matenco L, Krezsek C, Merten S, Schmid SM, Cloetingh S and Andriessen P** (2010) Characteristics of collisional orogens with low topographic built-up: an example from the Carpathians. *Terra Nova* **22**, 155–165.
- Matskiv BV, Pukach BD, Vorobkanych VM, Pastukhanova SV and Hnylko OM** (2009) State geological map of Ukraine. Scale 1: 200 000. Carpathian series. Sheets: M-34-XXXVI (Khust), L-34-VI (Baia Mare), M-35-XXXI (Nadvirna), L-35-I (Vichy De Sus) Kyiv, UkrDGRI, pp 185 (in Ukrainian).
- Mazur S, Aleksandrowski P, Gągała Ł, Krzywiak P, Żaba J, Gaidzik K and Sikora R** (2020) Late Palaeozoic strike-slip tectonics versus oroclinal bending at the SW outskirts of Baltica: case of the Variscan belt’s eastern end in Poland. *International Journal of Earth Sciences* **109**, 1133–1160.
- Młynarska M, Barnes C, Zack T, Majka J, Mazur S** (2024) In situ white mica Rb/Sr geochronology of the Leszczyniec metaigneous complex, West Sudetes: evidence of upper plate deformation at the onset of Variscan collision. *International Journal of Earth Sciences* **113**, 319–333.
- Molina JF, Moreno JA, Castro A, Rodrigues C and Fershtater GB** (2015) Calcic amphibole thermobarometry in metamorphic and igneous rocks: New calibrations based on plagioclase/amphibole Al-Si partitioning and amphibole/liquid Mg partitioning. *Lithos* **232**, 286–305.
- Munteanu M and Tatu M** (2003) The East-Carpathian Crystalline-Mesozoic Zone (Romania): Paleozoic amalgamation of Gondwana- and East European Craton-derived terranes. *Gondwana Research* **6**(2), 185–196.
- O’Sullivan G, Chew D, Kenny G, Henrichs I and Mulligan D** (2020) The trace element composition of apatite and its application to detrital provenance studies. *Earth-Science Reviews* **201**, 103044. <https://doi.org/10.1016/j.earscirev.2019.103044>.
- Oszczytko N, Oszczytko-Clowes M, Golonka J and Krobicki M** (2005) Position of the Marmarosh Flysch (Eastern Carpathians) and its relation to the Magura Nappe (Western Carpathians). *Acta Geologica Hungarica* **48**(3), 259–282.
- Paton C, Hellstrom J, Paul B, Woodhead J and Hergt J** (2011) Iolite: Freeware for the visualisation and processing of mass spectrometric data. *Journal of Analytical Atomic Spectrometry* **26**, 2508–2518.
- Paul AN, Spikings RA and Gaynor SP** (2021) U-Pb ID-TIMS reference ages and initial Pb isotope compositions for Durango and Wilberforce apatites. *Chemical Geology* **586**, 120604. <https://doi.org/10.1016/j.chemgeo.2021.120604>.
- Petrus JA and Kamber BS** (2012) VizualAge: a novel approach to laser ablation ICP-MS U-Pb geochronology data reduction. *Geostandards and Geoanalytical Research* **36**, 247–270.
- Plašienka D** (2012) Jurassic syn-rifting and Cretaceous syn-orogenic, coarse-grained deposits related to opening and closure of the Vahic (South

- Penninic) Ocean in the Western Carpathians – an overview. *Geological Quarterly* **56**(4), 602–628.
- Poprawa P, Malata T, Pécskay Z, Kusiak MA, Banaś M and Paszkowski M** (2006) Geochronology of the crystalline basement of the Western Outer Carpathians' source areas — constraints from the K/Ar dating of mica and Th–U–Pb chemical dating of monazite from the crystalline 'exotic' pebbles. *Geolines* **20**, 110–112.
- Powell R, White RW, Green ECR, Holland TJB and Diener JFA** (2014) On parameterizing thermodynamic descriptions of minerals for petrological calculations. *Journal of Metamorphic Geology* **32**, 245–260.
- Săndulescu M** (1984) Geotectonics of Romania (in Romanian). Editura Tehnică, Bucharest.
- Săndulescu M** (1988) Cenozoic tectonic history in the Carpathians. In *The Pannonian Basin: a study in basin evolution*. (eds L.H. Royden and F. Horvath F.), pp. 17–26. American Association of Petroleum Geologists Memoir no. 45.
- Săndulescu M** (1994) Overview on Romanian geology. ALCAPA II, Geological evolution of the Alpine-Carpathian-Pannonian system. Romanian Journal of Tectonics and Regional Geology, v. 75 (Suppl. 2), Bucharest. pp. 3–15.
- Schmid SM, Bernoulli D, Fügenschuh B, Matenco L, Scheffer S, Schuster R, Tischler M and Ustaszewski K** (2008) The Alpine-Carpathian-Dinaridic orogenic system: correlation and evolution of tectonic units. *Swiss Journal of Geosciences* **101**, 139–183.
- Schmitt AK and Zack T** (2012) High-sensitivity U–Pb rutile dating by secondary ion mass spectrometry (SIMS) with an O₂⁺ primary beam. *Chemical Geology* **332–333**, 65–73.
- Schoene B and Bowring SA** (2007) Determining accurate temperature-time paths in U–Pb thermochronology: An example from the SE Kaapvaal craton, southern Africa. *Geochimica et Cosmochimica Acta* **71**, 165–185.
- Schulz B** (2021) Petrochronology of monazite-bearing garnet micaschists as a tool to decipher the metamorphic evolution of the Alpine basement. *Minerals* **11**, 981. <https://doi.org/10.3390/min11090981>.
- Spears FS** (2010) Monazite–allanite phase relations in metapelites. *Chemical Geology* **279**, 55–62.
- Stacey JS and Kramers JD** (1975) Approximation of terrestrial lead isotope evolution by a two-stage model. *Earth and Planetary Science Letters* **26**, 207–221.
- Thomson SN, Gehrels GE, Ruiz J and Buchwaldt R** (2012) Routine low-damage apatite U–Pb dating using laser ablation–multicollector–ICPMS. *Geochemistry, Geophysics, Geosystem* **13**(2), Q0AA21. <https://doi.org/10.1029/2011GC003928>.
- Tkatchuk LG and Guržij DW** (1957) Rahovskij kristalličeskij massif (Karpaty). Akademija Nauk Ukrainskoj Sovjetskoj Respubliki, Kijev, pp. 1–124 (in Ukrainian).
- Uhlig V** (1907) Über die Tektonik der Karpathen. S.B. Academie des Wissenschaften, Wien **116**(1), pp. 871–982.
- Vodă A** (2002) Geologic, structural and metallogenetic map of the Crystalline-Mesozoic Zone of the Eastern Carpathians, scale 1:200 000. S.C. Prospectiuni S.A. Bucharest.
- von Raumer JF, Bussy F, Schaltegger U, Schulz B and Stampfli GM** (2013) Pre-Mesozoic Alpine basements - their place in the European Paleozoic framework. *Geological Society America Bulletin* **125**, 89–108.
- White RW, Powell R, Holland TJB, Johnson TE and Green ECR** (2014) New mineral activity-composition relations for thermodynamic calculations in metapelitic systems. *Journal of Metamorphic Geology* **32**, 261–286.
- White RW, Powell R and Johnson TE** (2014) The effect of Mn on mineral stability in metapelites revisited: new a-x relations for manganese-bearing minerals. *Journal of Metamorphic Geology* **32**, 809–828.
- Whitney DL and Evans BW** (2010) Abbreviations for names of rock-forming minerals. *American Mineralogist* **95**, 185–187.
- Zack T, Moraes R and Kronz A** (2004) Temperature dependence of Zr in rutile: empirical calibration of a rutile thermometer. *Contribution to Mineralogy and Petrology* **148**, 471–488.
- Zack T, Stockli DF, Luvizotto GL, Barth MG, Belousova E, Wolfe MR and Hinton RW** (2011) In situ U–Pb rutile dating by LA-ICP-MS: ²⁰⁸Pb correction and prospects for geological applications. *Contributions to Mineralogy and Petrology* **162**, 515–530.